



1 **Transport and storage of anthropogenic C in the Subpolar North Atlantic :**
2 **Model – Data comparison**
3 Virginie Racapé^{1,2}, Patricia Zunino³, Pascale Lherminier², Herlé Mercier³, Laurent Bopp^{1,4}, and
4 Marion Gehlen¹

6 ¹LSCE/IPSL, Laboratoire des Sciences du Climat et de l'environnement, CEA-CNRS-UVSQ, Orme
7 des Merisiers, Bât. 712, CEA/Saclay, 91190 Gif-sur-Yvette, Cedex, France

9 ²IFREMER, Laboratoire d'Océanographie Physique et Spatiale, UMR 6523, CNRS-IFREMER-
10 IRD-UBO, Plouzané, France

12 ³CNRS, Laboratoire d'Océanographie Physique et Spatiale, UMR 6523, CNRS-IFREMER-IRD-
13 UBO, Plouzané, France

15 ⁴Département de Géosciences, Ecole Normale Supérieure, 24 rue Lhomond 75005 Paris

17 **Corresponding author :** Virginie Racapé, virginie.racape@ifremer.fr

19 **Abstract**

20 The North Atlantic Ocean is a major sink region for anthropogenic carbon (Cant) and a major
21 contributor to its storage. While it is in general agreed that the intensity of the meridional
22 overturning circulation (MOC) modulates uptake, transport and storage of Cant in the North
23 Atlantic Subpolar Ocean, processes controlling their recent variability and 21st century evolution
24 remain uncertain. This study aims to investigate the relationship between the transport of Cant
25 across the Greenland-Portugal OVIDE section and the storage of Cant in the North Atlantic
26 Subpolar Ocean over the past 44 years. Its relies on the combined analysis of a multi-annual data set
27 (OVIDE program) and output from a global biogeochemical ocean general circulation model
28 (NEMO/PISCES) at ½° spatial resolution forced by the atmospheric reanalysis Drakkar Forcing Set
29 4. The skill of the model to reproduce observed physical and biogeochemical characteristics, as well
30 as their year-to-year variability is assessed over the period covered by observations. While the
31 analysis of the 44 year long hindcast simulation reveals that the interannual variability of the
32 storage rate of Cant is controlled by the northward transport during low NAO phases, as opposed to
33 the air-sea flux during strong NAO phases, the progressive and continuous increase of the subpolar
34 North Atlantic Cant inventory over the period 1958-2012 is driven by the regional uptake of Cant
35 from the atmosphere. Our results suggest thus an increase of the Cant inventory in this region over
36 the 21st century assuming unabated emissions of CO₂ and MOC fluctuation within observed
37 boundaries.



40 **1. Introduction**

41 Since the start of the industrial period and the subsequent rise of atmospheric CO₂, the ocean carbon
42 sink and the inventory of anthropogenic C (Cant) in the ocean have increase substantially (e.g.
43 Sabine et al., 2004; Le Quéré et al., 2009; 2014; Khatiwala et al., 2013). Overall, the ocean has
44 absorbed 28% of all anthropogenic CO₂ emissions, thus providing a negative feedback to global
45 warming and climate change (Ciais et al., 2013). Uptake and storage of Cant are, however,
46 characterized by a significant variability on interannual to decadal time scales (LeQuéré et al., 2015;
47 Wanninkhof et al., 2013) and any global assessment will hide important regional differences, which
48 prevents to detect correctly the change in oceanic sink [Séférian et al., 2014; McKinley et al., 2016].
49

50 The North Atlantic Ocean is a key region for Cant uptake (e.g. Sabine et al., 2004; Mikaloff-
51 Fletcher et al., 2006; Gruber et al., 2009) and stores currently as much as 20% of the total oceanic
52 inventory of 155±31 PgC (Khatiwala et al., 2013). Uptake and enhanced storage of Cant in this
53 region result from the combination of two processes: (1) winter deep convection in the Labrador
54 and Irminger Seas, which efficiently transfers Cant from surface waters to the deep ocean
55 (Kortzinger et al. 1999; Sabine et al., 2004; Pérez et al., 2008) and (2) the northward transport of
56 warm and Cant-laden tropical waters by the upper limb of the meridional overturning circulation
57 (MOC; e.g. Álvarez et al., 2004; Mikaloff-Fletcher., 2006; Gruber et al., 2009; Pérez et al., 2013).
58 Both terms, deep water formation and circulation, are characterized by high temporal variability in
59 response to the leading mode of atmospheric variability in the North Atlantic, the North Atlantic
60 Oscillation (NAO). Hurrell (1995) defined the NAO index as the normalized sea-level pressure
61 difference in winter between Azores and Iceland. A positive (negative) NAO phase is thus
62 characterized by a high (low) pressure gradient between these two systems coupled to strong (weak)
63 westerly winds in the subpolar region. Between the mid-1960s and the mid-1990s, the North
64 Atlantic evolved from a negative to positive NAO phase. The change in wind conditions induced an
65 acceleration of the North Atlantic Current (NAC), as well as increased heat loss and vertical mixing
66 in the subpolar gyre (e.g. Dickson et al., 1996; Curry and McCartney, 2001; Sarafanov, 2009;
67 Delworth and Zeng, 2015). Concomitant enhanced deep convection led to the formation of large
68 volumes of Labrador Sea water (LSW) with a high load of Cant (Lazier et al., 2002; Pickart et al.,
69 2003; Pérez et al., 2008; 2013). Between 1997 and the yearly 2010's, the region undergoes a decline
70 in NAO index. This has caused a reduction of LSW formation (Yashayaev, 2007; Rhein et al., 2011)
71 and a slowing-down of the northward transport of subtropical water by the NAC (Häkkinen and
72 Rhines, 2004; Bryden et al., 2005; Pérez et al., 2013). As a result, the increase in the subpolar Cant
73 inventory is below that expected from rising atmospheric anthropogenic CO₂ levels alone



74 (Steinfeldt et al., 2009; Pérez et al., 2013).

75

76 Based on the analysis of a time series of physical and biogeochemical properties between 1997 and
77 2006, Pérez et al. (2013) propose that Cant storage rates in the subpolar gyre are primarily
78 controlled by the MOC intensity. A reduction in the MOC intensity would thus lead to a decrease in
79 Cant storage and would give rise to a positive climate-carbon feedback. The importance of MOC in
80 modulating the North Atlantic Cant inventory was previously suggested by model studies. Those
81 projected a decrease in the North Atlantic Cant inventory over the 21st century in response to a
82 projected MOC slow-down under future climate warming (Crueger et al., 2008). Based on the same
83 sections than Pérez et al. (2013), Zunino et al. (2014) extended the time window of analysis to
84 1997-2010 and have proposed a novel proxy for Cant transport. It is defined as the difference of the
85 Cant concentration between the upper and the lower limbs of the overturning circulation times
86 MOC intensity (see section C in Supplement for a model-based discussion of the proxy). They
87 observed that while the multi-annual variability of transport of Cant was controlled by the
88 variability of MOC intensity, its long-term change could depend on the increase in Cant
89 concentration in the upper limb of the MOC. As the latter reflects uptake of Cant through air-sea gas
90 exchange at the atmosphere-ocean boundary, it questions the dominant role of ocean dynamics in
91 controlling Cant storage in the subpolar gyre (Pérez et al., 2013). If the storage rate of Cant in the
92 subpolar gyre is indeed at first order controlled by the load of Cant in the upper limb of the MOC,
93 the subpolar Cant inventory is expected to increase along with increasing atmospheric CO₂ - albeit
94 not necessarily at the same rate - and to provide a negative feedback on rising atmospheric CO₂
95 levels over the 21st century.

96

97 The objective of the present study is to evaluate the relationship between Cant transport, air-sea
98 fluxes and storage rate in the Subpolar North Atlantic, along with their combined evolution over the
99 past 44 years (1958-2012). It relies on the combination of a multi-annual data set gathered along the
100 OVIDE section (Mercier et al., 2015) and output from the global biogeochemical ocean general
101 circulation model NEMO/PISCES at 1/2° spatial resolution forced by the atmospheric reanalysis
102 Drakkar Forcing set 4 (DFS4, Bourgeois et al., 2016).

103

104 **2. Material and methods**

105 **2.1. NEMO-PISCES model**

106 This study is based on a global configuration of the ocean model system NEMO (Nucleus For
107 European Modelling of the Ocean) version 3.2 (Madec, 2008). The quasi-isotropic tripolar grid



108 ORCA (Madec and Imbard, 1996) has a resolution of 0.5° in longitude and $0.5^\circ \times \cos(\phi)$ in latitude
109 (ORCA05) and 46 vertical levels with 10 levels in the upper 100m. It is coupled online to the
110 Louvain-la-Neuve sea ice model version 2 (LIM2) and the biogeochemical model PISCES-v1
111 (Pelagic interaction Scheme for Carbon and Ecosystem studies; Aumont and Bopp, 2006).
112 Parameter values and numerical options for the physical model follow Barnier et al. (2006) and
113 Timmermann et al. (2005). Two atmospheric reanalysis products, DFS4.2 and DFS4.4, were used
114 for this study. DFS4.2 is based on ERA-40 (Brodeau et al., 2010) and covers the period 1958-2007
115 while DFS4.4 is based on ERAInterim and covers 2002-2012 (Dee et al., 2011). The simulation was
116 spun up over a full DFS4.2 forcing cycle (50 years) starting from rest and holding atmospheric CO_2
117 constant to 1870 levels (284 ppm). Temperature and salinity were initialized as in Barnier et al.
118 (2006). Biogeochemical tracers were either initialized from climatologies (nitrate, phosphate,
119 oxygen, dissolved silica from the 2001 World Ocean Atlas, Conkright et al. (2002); preindustrial
120 dissolved inorganic carbon (DIC) and total alkalinity (Alk) from GLODAP, Key et al. (2004)), or
121 from a 3000 year long global NEMO/PISCES simulation at 2° horizontal resolution (Iron and
122 dissolved organic carbon). The remaining biogeochemical tracers were initialized with constant
123 values.

124 At the end of the spin-up cycle, two 143-year long simulations were started in 1870 and run in
125 parallel. The first one, the historical simulation, was forced with spatially uniform and temporally
126 increasing atmospheric CO_2 concentration (Le Quéré et al., 2014) whereas in the second one, the
127 control simulation, the mole fraction of CO_2 was kept constant in time at 1870 level. Both runs were
128 forced by repeating 1.75 cycles of DFS4.2 interannually varying forcing over 1870 to 1957. Then
129 DFS4.2 was used from 1958 to 2007. Simulations were extended from 2002 to 2012 by switching
130 to DFS4.4. No significant differences were found in tracer distributions and Cant related quantities
131 between both atmospheric forcing products during the years of overlap (2002-2007). Carbonate
132 chemistry and air-sea CO_2 exchanges were computed by PISCES following the Ocean Carbon
133 Cycle Model Intercomparison Project protocols (www.ipsl.jussieu.fr/OCMIP) and the gas transfer
134 velocity relation provided by Wanninkhof (1992). Cant concentrations and anthropogenic CO_2
135 fluxes were calculated as the difference between historical (total C) minus control (natural C
136 component) simulations. The global ocean inventory of Cant simulated by the model in 2010
137 amounted to 126 PgC. It is at the lower end of the uncertainty range of the estimate by Khatiwala et
138 al. (2013) of 155 ± 31 PgC (Fig. 1). At the global scale, the error of the model is close to 6% (values
139 excluding arctic regions and margin seas). The mismatch between the modeled Cant inventory and
140 that of Khatiwala et al. (2013) is largely explained by the difference in the starting year of
141 integration: 1870 for this study as opposed to 1765 in Khatiwala et al. (2013). The coupled model



142 configuration is referred to as ORCA05-PISCES hereafter. The reader is invited to refer to
143 Bourgeois et al. (2016) for a detailed description of model and simulation strategy.
144
145 This study followed a two-step approach. The model was first evaluated against the OVIDE data set
146 from year 2002 to 2010 (DFS4.4). The data set consists of observations for June only (see below).
147 As the water column distribution of hydrological and biogeochemical properties are comparable
148 between May and July, model output was subsampled along the section in June for a comparison to
149 data (Tables 1 and 2). Next, the period of study is extended to 1958-2012 (DFS4.4 up to 2001;
150 DFS4.4 over 2002 to 2012) to study the long-term variability of the Cant fluxes, storage and budget.

151

152 2.2. OVIDE data set

153 Observations used to evaluate model output from ORCA05-PISCES in the North Atlantic Ocean
154 were collected within the framework of the OVIDE program. The program aims to document and
155 understand the origin of the interannual to decadal variability in circulation and properties of water
156 masses in the Subpolar North Atlantic in the context of climate change ([http://www.umr-
158 lops.fr/Projets/Projets-actifs/OVIDE](http://www.umr-
157 lops.fr/Projets/Projets-actifs/OVIDE)). Since 2002, one spring-summer cruise is run every two years
159 (Table 1) between Greenland and Portugal following the track presented on figure 2. Dynamical
160 (ADCP), physical (Temperature -T- and Salinity -S-) and biogeochemical (e.g. Alk, pH, dissolved
161 oxygen -O₂- and nutrients) properties are sampled during each cruise at full depth hydrographic
162 stations spaced by 25 nautical miles (NM) and reduced to 16 NM in the Irminger sea and 12 NM or
163 less over steep topographic features. An overview of instruments, analytical methods and accuracies
164 of each parameter is summarized in Zunino et al. (2014). pH and Alk are used to calculate the
165 concentration of DIC following the recommendations and guidelines from Velo et al. (2010). DIC is
166 used in turn together with T, S, nutrients, O₂ and Alk to derive the Cant concentration following the
167 ϕ CT method (Pérez et al., 2008; Vázquez-Rodríguez, 2009). This data-based diagnostic approach
168 uses water mass properties of the subsurface layer between 100-200m as reference to evaluate
169 preformed and disequilibrium conditions. The random propagation of errors associated with input
170 parameters yields an uncertainty of 5.2 $\mu\text{mol kg}^{-1}$ on C_T values (Pérez et al., 2010). The OVIDE
171 data set is available for the period 2002-2010 on the CARINA website
(<http://cdiac.ornl.gov/oceans/CARINA/>; Table 1).

172

173 2.3. Diagnostic of Cant transport and budget

174 *Transport of Cant across a section*

175 The simulated transport of Cant (T_{Cant}) across a section is evaluated either from online or from



176 offline diagnostic for each ORCA05 grid-level. The transport of Cant is then integrated vertically
 177 from bottom to surface and horizontally from the beginning (A) to the end (B) of a section along a
 178 continuous line defined by zonal (y) or meridional (x) grid segment (Fig. S1). Positive values stand
 179 for northward and/or eastward transport (see section A in Supplement for the description of section).

180

181 In the online approach, the transport of Cant (${}^mT_{Cant}^{online}$) is the sum of the advection (${}^mT_{Cant}^{adv}$), the
 182 diffusion (${}^mT_{Cant}^{lf}$) and the eddy (${}^mT_{Cant}^{eiv}$) contribution (Eq. (1)). The ${}^mT_{Cant}^{adv}$ term corresponds to
 183 the product of velocities orthogonal to the section (V) times Cant concentration ($[Cant]$). The
 184 ${}^mT_{Cant}^{lf}$ term is the transport of Cant due to the horizontal diffusion. Finally, the ${}^mT_{Cant}^{eiv}$ term is the
 185 transport of Cant due to eddies; it is based on the use of Gent and McWilliams (1990)
 186 parameterization. All these terms are diagnosed online and averaged over 5-days for the period
 187 2003-2011.

$$188 \quad {}^mT_{Cant}^{online} = \left[{}^mT_{Cant}^{adv} + {}^mT_{Cant}^{lf} + {}^mT_{Cant}^{eiv} \right]^{online} \quad (1)$$

189

190 In the offline approach, Cant transport is reduced to the advective component because the
 191 contribution of diffusion and eddies are negligible for sections studied in the model (see Fig. S2)
 192 that echoes results from Treguier et al. (2006) for the OVIDE section. Evaluation of the advective
 193 transport of Cant is based on 1) monthly averaged model output over the period 2002-2010 to
 194 compare to observation-based results along the OVIDE section (Zunino et al., 2014), and 2) yearly
 195 averaged model output over the period 1958-2012 to study the long-term variability of Cant fluxes
 196 and storage rates. This last evaluation is completed by the heat transport. It is evaluated in
 197 ORCA05-PISCES simulations from velocities orthogonal to the section (V) and the heat term
 198 provided by the international thermodynamic equations of seawater (TEOS 2010).

199

200 Budget of Cant in the North Atlantic Ocean

201 The budget of Cant is computed for three North Atlantic regions (see below for definition of
 202 regions). This budget is defined as the balance between i) the time rate of change in Cant, vertically
 203 and horizontally integrated, ii) the incoming and outgoing transport of Cant across boundaries of
 204 each region and iii) the anthropogenic air-sea CO_2 exchange, spatially integrated. This is then
 205 completed by the heat transport for the period 2003-2011. All terms are estimated from model
 206 output either from monthly or yearly averages depending on the period analyzed (monthly for 2003-
 207 2011; yearly for 1958-2012). Finally, relationships between Cant fluxes and its storage rate are
 208 investigated for each region. A moving average (windows: 12 month for 2003-2011, 10 years for
 209 1958-2012) has been used beforehand for the smoothing of times series data, followed by a least-



210 square fit to remove linear trend. Results of smoothing are displayed on Fig. S3.

211

212 3. **Model evaluation over the OVIDE period**

213 3.1. **Distribution of hydrological and biogeochemical parameters along the Greenland- 214 Portugal OVIDE section**

215 Figure 3 illustrates the distribution of salinity (a and b), dissolved oxygen (c and d) and dissolved
216 silica (e and f) concentrations along the Greenland-Portugal OVIDE section, as simulated by
217 ORCA05-PISCES (a, c and e) and compared to the OVIDE data set (b, d and f). The distributions
218 of these hydrological and biogeochemical tracers are characterized by typical regional features
219 which reflect the origin and properties of water masses. These regional features are particularly
220 useful for the validation of model simulations.

221 The highest salinity along the section is found in surface and subsurface waters of the Eastern North
222 Atlantic and Iberian basin (east of 1500 km, Fig. 3b). It corresponds respectively to East North
223 Atlantic Central Water (ENACW) and to Mediterranean Water (MW) (Harvey, 1982; Tsuchiya et
224 al., 1992; Pollard et al., 1996, van Aken and Becker, 1996, Álvarez et al., 2004). While these
225 properties are well reproduced by the model (Fig. 3a), simulated salinity maxima are either
226 underestimated for MW ($S^{\text{ORCA05}} > 35.6$ vs $S^{\text{OVIDE}} > 36.1$, García-Ibáñez et al., 2015; Fig. 3a) or lack
227 the expected distribution for ENACW (values too high or too small compared to observations).
228 There is another core of relatively high salinity in both the OVIDE data (Fig. 3b) and the model
229 output (Fig. 3a). It is located in the subsurface water over the Reykjanes Ridge and reflects the
230 influence in the subpolar region of the saltier central Atlantic water carried by the Eastern
231 Reykjanes Ridge Current (ERRC) derived from the NAC (Pickart et al., 2005; Våge et al., 2011;
232 Daniault et al., 2016).

233

234 In the water column, two cores of relatively low salinity and high O₂ concentration are identifiable
235 on both sides of the Reykjanes Ridge in the OVIDE data (Fig. 3d). They are reproduced by
236 ORCA05-PISCES (Fig 3c), albeit with lower levels than the in-situ data ($O_2^{\text{ORCA05}} > 260 \mu\text{mol kg}^{-1}$
237 vs $O_2^{\text{OVIDE}} = 285 \pm 2 \mu\text{mol kg}^{-1}$, García-Ibáñez et al., 2015). They are consistent with the two
238 pathways of LSW (Pickart et al., 2003; Alvarez et al., 2004; Daniault et al., 2016) and take up the
239 largest volume of water of the section like in García-Ibáñez et al. (2015).

240

241 High dissolved silica (Si(OH)₄) concentrations below 2500m depth in the Iberian basin (Fig. 3f)
242 correspond to the lower limb of North-East Atlantic Deep Water (NEADWI), which is
243 predominantly formed by the mixing between the recirculation of Iceland-Scotland Overflow Water



244 (ISOW), rich in oxygen, and the Antarctic Bottom Water (AABW), poor in oxygen but rich in
245 $\text{Si}(\text{OH})_4$ (van Aken and Beker, 1996; van Aken et al., 2000, García-Ibáñez et al., 2015). In the
246 model, the $\text{Si}(\text{OH})_4$ signal characteristic of NEADW is identified in the same location, but it is
247 stronger and associated to a lower oxygen concentration compared to OVIDE ($\text{Si}(\text{OH})_4^{\text{ORCA05}} > 55$
248 $\mu\text{mol kg}^{-1}$ vs $\text{Si}(\text{OH})_4^{\text{OVIDE}} < 50 \mu\text{mol kg}^{-1}$, Figs. 3e and f; $\text{O}_2^{\text{ORCA05}} < 200 \mu\text{mol kg}^{-1}$ vs $\text{O}_2^{\text{OVIDE}} >$
249 $230 \mu\text{mol kg}^{-1}$, Figs. 3b and c). Moreover, high values of simulated dissolved silica concentrations
250 are found in the deep Iceland and Irminger basins, contrasting with observations. Both basins are
251 generally occupied at depth by Denmark Strait Overflow Water (DSOW) and by ISOW. Recently
252 ventilated in the Arctic region (Rhein et al., 2002; Tanhua et al., 2005), DSOW and ISOW result
253 from a complex mixture of various water masses and flow over the bottom along the Greenland
254 continental slope and on both sides of the Reykjanes Ridge (Tanhua et al., 2005; Yashayaev et
255 Dickson, 2008; García-Ibáñez et al., 2015). The DSOW is traced by its maximum in O_2 ($>280 \mu\text{mol}$
256 kg^{-1} , Rhein et al., 2002; García-Ibáñez et al., 2015) and its relative minimum in nutrients (< 15
257 $\mu\text{mol kg}^{-1}$, Fig. 3c; Tanhua et al., 2005), whereas the ISOW is characterized by a relative maximum
258 in salinity (close to 35, García-Ibáñez et al., 2015). The comparison between observed (Figs. 3b, d
259 and f) and simulated (Figs. 3a, c and e) properties suggests that the model fails to correctly
260 reproduce dense overflows. The underestimation of DSOW and ISOW by the model results in a
261 predominant contribution of water masses coming from the Antarctic to deep waters in the Iceland
262 and Irminger basins.

263

264 3.2. Mass transport across the Greenland-Portugal OVIDE section

265 Figure 4 illustrates the monthly evolution of the net volume transport across the Greenland-Portugal
266 OVIDE section from model simulations over the period 2002-2010. Values vary between -0.46 Sv
267 ($1 \text{ Sv} = 10^6 \text{ m}^3 \text{ s}^{-1}$) and 1.88 Sv without any clear and obvious seasonal cycle. As expected, the net
268 transport is towards the North (Lherminier et al., 2007; Mercier et al., 2015) with a mean annual
269 flow of $0.67 \pm 0.46 \text{ Sv}$. Compared to estimates derived from the OVIDE data set for the month of
270 June, the model simulates a net transport in line with these estimates for June 2002 and 2004, but
271 underestimates the net transport by up to 50% for June 2006 and 2008, respectively and by up to
272 120% for June 2010 (Table 2). Considering the large modeled month-to-month variability of net
273 transport, the model misfit could correspond to a slight phase shift between modeled and true yet
274 unresolved variability. If indeed the net transport is as variable as suggested by ORCA05-PISCES
275 on sub-seasonal to interannual time scales, then observation-based estimates derived for June only
276 would not represent the annual mean value. This is confirmed for the model by an independent two
277 samples t-test, which rejects the null hypothesis of the averaged-mass transport computed for the



278 month of June (0.19 ± 0.33 Sv; Table 2) being representative of the annual mean.
279

280 The computation of mass transport using a meridional overturning stream function (see section C in
281 Supplement for details) reveals a vertical and horizontal accumulated arrangement in ORCA05-
282 PISCES in relative agreement with the OVIDE data set (Fig. 5). The model does, however, not
283 reproduce the interannual variability present in observations (Figs. 5a and 5b). Moreover, it
284 underestimates the magnitude of MOC by around 2 Sv (with a model estimate at 13.4 ± 0.6 Sv vs
285 15.5 ± 2.3 for OVIDE-based estimate, Mercier et al., 2015; Table 2). The upper limb of the MOC, the
286 NAC (Lherminier et al., 2010), flows northeastward in the Eastern part of the section (East of 1100
287 km; Fig. 5b), with its modified branch, the Irminger Current, in the Western part (around 700km off
288 the Greenland Coast) in model and data as defined by Mercier et al. (2015) (Fig. 5b). The NAC is
289 simulated with a lower variability and weaker intensity (Fig. 5b; ORCA05-PISCES increase in
290 cumulative mass transport of 15 Sv instead of 25 Sv between 1100km and 2500km from Greenland
291 coast). In addition, the vertical stream function (Fig. 5a) reveals a stronger current between the
292 surface and the density anomaly (σ_1) 31.5 kg m^{-3} in the model, only observed at the east of the
293 Reykjanes Ridge (not show here). This overestimation of the overturning stream function in the
294 model is likely due to a shift in the position of the Western limit of the NAC. The Western limit is
295 detected close to zero values for mass transport. It occurs around 1000 km off Greenland in the
296 model, instead of 1300 km in observations (Fig. 5b).

297 The lower limb of MOC, mainly related to the Western Boundary Current (WBC), flows southward
298 in the western part of the section (Lherminier et al., 2007; 2010; Mercier et al., 2015). Sigma 1
299 separating both limbs of the MOC simulated by the model is lower ($32.01 \pm 0.01 \text{ kg m}^{-3}$) than those
300 estimated with in situ data (32.14 kg m^{-3}). It follows that the lower (upper) limb in the model takes
301 up a bigger (smaller) volume along the section in the model compared to the OVIDE data set (Fig.
302 6). The model underestimates the intensity of the southward transport of the WBC in the Irminger
303 Sea, and the ERRC in the Iceland basin (Fig. 5b), which are the most intense currents flowing in the
304 lower limb of the MOC. It also underestimates the cumulative mass transport for $\sigma_1 > 32.40 \text{ kg m}^{-3}$
305 ($\sigma_0 > 27.7 \text{ kg m}^{-3}$), which is close to 0 Sv in the model (Fig. 5a) as opposed to 7 Sv recorded by
306 Lherminier et al. (2007) and García-Ibáñez et al. (2015). These densest water masses correspond to
307 NEADWI, DSOW and ISOW. Taken together, the misfit between observation-derived estimates and
308 modeled mass transport being the largest in the Irminger and Iceland basins and the preceding
309 discussion of biogeochemical properties (III.1) suggest that the significant underestimation of mass
310 transport in the highest density classes is probably due to the close to zero contribution of overflow
311 waters to the transport in the model at the latitude of the OVIDE section.



312 Finally, mean values of the magnitude of the MOC computed for the month of June from model
313 output over the period 2002-2010 are equal to the annual average computed over the same period
314 (two sampled t-test; 13.4 ± 2.4 Sv, Table 2). However, its variability computed as the standard
315 deviation of June estimates (± 0.6 Sv) is not representative for its variability in ORCA05-PISCES
316 when computed over the full period (± 2.4 Sv, Table 2).

317

318 **3.3. Cant distribution along the Greenland-Portugal OVIDE section**

319 Concentrations of Cant computed by the model or from the OVIDE data set represent estimates
320 derived by two inherently different approaches: the former is the difference between two
321 simulations (historical minus control), the latter is computed following the ϕ CT method (sections
322 II.1 and II.2). Both methods yield comparable distributions along the OVIDE section with higher
323 concentrations in surface waters and lower levels at depth (Figs. 6a and 6b). The surface to depth
324 gradient is more pronounced in the Eastern basin. The two LSW cores, relatively rich in Cant, are
325 present on both sides of the Reykjanes Ridge. During the OVIDE period, values simulated by
326 ORCA05-PISCES are nevertheless lower by $6.3 \pm 0.6 \mu\text{mol kg}^{-1}$ compared to observed-based
327 estimates (Table 2). This deficit is more pronounced in the upper limb of MOC ($\Delta\text{Cant}^{\text{model-data}} = -$
328 $5.9 \pm 0.7 \mu\text{mol kg}^{-1}$) than in the lower limb ($\Delta\text{Cant}^{\text{model-data}} = -3.6 \pm 0.6$, Table 2). The largest
329 difference between model and data, up to $-20 \mu\text{mol kg}^{-1}$ (Fig. 6c), is detected in the subsurface
330 waters at the transition between ENACW and MW and between both limbs of the MOC. Its
331 interannual variability (standard deviation (of model-data) up to $10 \mu\text{mol kg}^{-1}$; Fig. 6d) is also
332 largest at the boundary between upper and lower limbs of the MOC, mainly between 700 km to
333 2000 km off Greenland. The higher interannual variability in this region could be explained by the
334 interannual variability of the NAC intensity, which is underestimated by ORCA05-PISCES.
335 Moreover, this region is also a potential area for mode water formation (de Boissésion et al., 2012),
336 but this processus has not been studied in this paper. It is not the scope of this paper. Figure 6 also
337 reveals an underestimation by the model of Cant levels in NEADWI by 5 to $10 \mu\text{mol kg}^{-1}$ which is
338 in line with a close to zero contribution of dense Cant rich overflow waters along the OVIDE
339 section.

340

341 **3.4. Budget of Cant in the North Atlantic Ocean (north of 25° N)**

342 Figure 7 summarizes the budget of Cant in the North Atlantic simulated by the model over the
343 period 2003-2011. In order to facilitate the comparison of the modeled budget to Pérez et al. (2013),
344 we defined two boxes separated by the Greenland-Portugal OVIDE section. The first one extends



345 from 25° N to the OVIDE section; the second box extend from the OVIDE section to the Nordic
346 sills. Seasonality was removed beforehand using a 12-month running filter (section II.3).
347
348 In the model, over one third of Cant entering in the southern box at 25° N (0.092 ± 0.016 PgC yr⁻¹) is
349 transported across the OVIDE section (0.035 ± 0.005 PgC yr⁻¹) and leaves the domain at the Nordic
350 sills (0.034 ± 0.004 PgC yr⁻¹). The latter corresponds to a net northward transport resulting from a
351 northwards flux across the Iceland-Scotland strait (0.053 ± 0.005 PgC yr⁻¹) and a southward flux
352 across the Denmark strait (-0.020 ± 0.014 PgC yr⁻¹). The remainder of the regional Cant storage is
353 provided by the air to sea exchange with the largest values south of the OVIDE section (South:
354 0.156 ± 0.008 PgC yr⁻¹; North 0.044 ± 0.003 PgC yr⁻¹). As a consequence, 88% of the incoming Cant
355 flux (computed as $(0.092 + 0.156 + 0.044 - 0.034) / (0.092 + 0.156 + 0.044)$; Fig. 7) is stored inside the
356 region every year, predominantly south of the OVIDE section (South : 0.216 ± 0.019 PgC yr⁻¹ ; North
357 : 0.045 ± 0.006 PgC yr⁻¹).

358 Compared to the previous studies of Pérez et al. (2013) and Zunino et al. (2014; 2015a and b), the
359 transport of Cant is three time smaller at 25° N and the OVIDE section and two time smaller at the
360 sills. From our discussion in sections III.2 and III.3, it follows that the underestimation of Cant
361 transport in ORCA05-PISCES is likely due to the underestimation of both circulation and Cant
362 concentration. The hypothesis is supported by the analysis of the heat transported from southern
363 latitudes at 25° N and the OVIDE section which is also underestimated by the model (Fig. 7)
364 compared to Pérez et al (2013). Pérez et al. (2013) estimated 1.10 ± 0.01 PW and 0.59 ± 0.09 PW at,
365 25° N and OVIDE respectively, while the model yields a corresponding heat transport of 0.78 ± 0.06
366 PW and 0.39 ± 0.02 PW. The discrepancy between model and observation-based estimates of heat
367 transport is, however, not as large as for ${}^mT_{\text{Cant}}^{\text{adv}}$, probably due to a better simulation of temperature
368 than Cant concentration by the model (mean model-data bias along the section: $-0.4 \pm 0.9^\circ\text{C}$ for a
369 mean value of 5°C (8% of error) for temperature, $7 \mu\text{mol kg}^{-1}$ for a mean value of $25.4 \mu\text{mol kg}^{-1}$
370 (27%) for Cant). The underestimation of meridional heat transport by the model reflects thus
371 predominantly the weak MOC (Mercier et al., 2015). The comparison between biases in ${}^mT_{\text{Cant}}^{\text{adv}}$
372 and heat transport highlights the contribution of both circulation and Cant concentration in setting
373 the discrepancy between observed and modelled meridional transport of Cant. Concerning the air-
374 sea flux of Cant, the model estimates are larger than those derived from in situ data: Southern box:
375 model = 0.156 ± 0.008 PgC yr⁻¹, Pérez et al. (2013) = 0.12 ± 0.05 PgC yr⁻¹; Northern box: model =
376 0.044 ± 0.003 PgC yr⁻¹, Pérez et al. (2013) = 0.016 ± 0.012 PgC yr⁻¹. The overestimation of air to sea
377 anthropogenic CO₂ fluxes in the model could be due to the underestimation of Cant concentration in
378 the ocean by the model, which increases the Cant gradient between the atmosphere and the ocean



379 and ultimately enhances the estimate of Cant uptake by the ocean. Finally, storage rates of Cant
380 estimated for the period 2003-2011 are close to results from Pérez et al. (2013), referenced to 2004:
381 Southern box: model = 0.216 ± 0.019 , Pérez et al. (2013) = 0.280 ± 0.011 ; Northern box: model =
382 0.045 ± 0.006 and Pérez et al. (2013) = 0.045 ± 0.004 PgC yr⁻¹.

383

384 We derive the contribution of air-sea uptake and transport of Cant to the variability of the North
385 Atlantic Cant inventory from the analysis of multi-annual time series of air-sea Cant fluxes, the
386 transport divergence of Cant (defined as the difference between incoming and outgoing Cant fluxes
387 computed at the borders of boxes) and Cant storage rate for each box. Time series were smoothed as
388 explained previously and the potential trends were removed as noted in section II.3. Correlation
389 coefficient (r), p -value and Coefficient of determination (r^2) are summarized in table 3. Our results
390 suggest that, over the period 2003-2011, the rate of Cant storage between 25° N and the Nordic sills
391 is strongly correlated with the northward transport of Cant-laden waters coming from South of 25°
392 N (25° N: $r = 0.96$, p -value = 0.00; OVIDE: $r = 0.95$, p -value = 0.00), which explains 89%
393 (OVIDE) to 93% (25° N) of its interannual variability. The dominance of transport over gas
394 exchange is corroborated by observation-based assessments (Pérez et al., 2013; Zunino et al., 2014;
395 2015a and b).

396

397 The evaluation of model output against hydrological and biogeochemical observations, as well as
398 the assessment of drivers of the temporal variability of Cant transport, air to sea fluxes and storage
399 rates leads to the conclusion that major controls of the Cant budget and of its variability are well
400 reproduced by the model for the period 2003-2011, despite the underestimation of absolute Cant
401 concentrations and meridional circulation.

402

403 **4. Long-term change in Cant fluxes and storage rate in the Subpolar North Atlantic region**

404 In this section, we extend the analysis to the full simulation period (1958-2012) with the objective
405 to better understand 1) the relative contribution of the variability of circulation and the increase in
406 Cant concentration to the variability of Cant transport through the North Atlantic Ocean, and 2) the
407 long-term change of the Cant inventory in this region as well as driving processes. For this section,
408 the study area is limited to the mid-latitude and subpolar North Atlantic region and extends from
409 36° N (instead of 25° N, which includes the northern part of the subtropical region) to the Nordic
410 sills (Mikaloff-Fletcher et al., 2003). The transport of Cant over the Nordic sills corresponds to the
411 closure term of the regional budget.

412



413 **4.1. Contribution of variability of both circulation and Cant accumulation on Cant**
 414 **transport variability**

415 Figure 8 presents annual time series (1958-2012) of the magnitude of MOC and the transport of
 416 heat and Cant at 36° N and across the OVIDE section. While between 57% (OVIDE, $r=0.76$, p -
 417 value = 0.00) and 81% (36° N, $r=0.90$, p -value = 0.00) of the variance of ${}^mT_{\text{HEAT}}^{\text{adv}}$ over the study
 418 period is explained by the variability of MOC_σ , it resolves only 44% of the variance of ${}^mT_{\text{Cant}}^{\text{adv}}$ at
 419 36° N and no significant relationship is found at the OVIDE section ($r=0.02$, p -value = 0.90). The
 420 circulation is thus the major mechanism driving the inter-annual to decadal variability of the heat
 421 content transferred across both sections. Its impact on the variability of Cant transport is, however,
 422 masked by several other mechanisms. Figure 8 reveals that ${}^mT_{\text{Cant}}^{\text{adv}}$ is characterized by a significant
 423 and continuous increase from $0.009 \pm 0.001 \text{ PgC yr}^{-1}$ in 1958-60 to $0.050 \pm 0.018 \text{ PgC yr}^{-1}$ in 2010-12
 424 at 36° N and from $0.008 \pm 0.001 \text{ PgC yr}^{-1}$ to $0.043 \pm 0.005 \text{ PgC yr}^{-1}$ at the OVIDE section. This large
 425 increase is neither detected on ${}^mT_{\text{HEAT}}^{\text{adv}}$ ($0.0016 \pm 0.0004 \text{ PW yr}^{-1}$ at 36° N and $0.0003 \pm 0.0002 \text{ PW}$
 426 yr^{-1} at OVIDE) nor on MOC_σ ($0.015 \pm 0.006 \text{ sv yr}^{-1}$ at 36° N and $0.003 \pm 0.007 \text{ sv yr}^{-1}$ at OVIDE),
 427 nor on the net volume of water transported across both sections ($0.001 \pm 0.001 \text{ sv yr}^{-1}$ at 36° N and -
 428 $0.000 \pm 0.003 \text{ sv yr}^{-1}$ at OVIDE). The latter (net mass transport) implies an equivalent evolution
 429 (increase or decrease) of circulation strength in the upper and the lower limb of the MOC. It follows
 430 that the increase in the northward transport of Cant (${}^mT_{\text{Cant}}^{\text{adv}}$) since 1958 is due to the increase in
 431 Cant concentration in the upper limb of the MOC as suggested by Zunino et al. (2014). In order to
 432 isolate the effect of circulation, we removed the positive trend from ${}^mT_{\text{Cant}}^{\text{adv}}$. The relationship
 433 between the detrended ${}^mT_{\text{Cant}}^{\text{adv}}$ and the magnitude of MOC (36° N : $r^2 = 0.51$; OVIDE : $r^2 = 0.02$)
 434 does not change over the period of analysis, thus suggesting that a third mechanism, air sea Cant
 435 fluxes, has a relevant role on the variability of northward transport of Cant in the subpolar North
 436 Atlantic region.

437

438 **4.2. Long-term change in Cant storage rate and driving processes**

439 In order to assess the long-term change in Cant storage rate in the Subpolar North Atlantic and to
 440 identify underlying drivers, we focus on three well-documented periods of the last decades
 441 corresponding to NAO phases. In the model, the response of the ocean to leading mode of North
 442 Atlantic climate variability is detected from interannual anomalies of the MOC intensity at the
 443 OVIDE section (Fig.9). The anomaly of MOC intensity is a good indicator of regional circulation
 444 strength with negative anomaly for low MOC intensity, positive anomaly for high MOC intensity
 445 (Desbruyères et al., 2013). The first period is defined by negative MOC_σ anomalies from 1967 to
 446 1977 during the low NAO event of the mid-1960s (Hurrell et al., 1995). The second period is



447 characterized by predominantly positive values between 1985 and 1997 and corresponds to the
448 strong NAO event of the mid-1990s (Hurrell et al., 1995; Osborn, 2006). The third period is
449 associated with low NAO once again (Osborn 2006; 2011) and a significant decrease in MOC
450 intensity since 2002. To identify processes driving the long term change in Cant storage rate,
451 modeled time series are smoothed with a 10 year time-window and positive trends are removed
452 (section II.3, Fig. S3). As a consequence, time series are reduced to the period 1964-2006.
453

454 Figure 10 provides the budget of Cant for two boxes, North and South of the OVIDE section. In
455 both regions, the significant increase in MOC intensity recorded between 1967-77 (low NAO phase;
456 36° N: 11.1 ± 0.1 Sv; OVIDE: 12.5 ± 0.2 Sv) and 1985-97 (strong NAO phase; 36° N: 11.8 ± 0.2 Sv;
457 OVIDE : 13.3 ± 0.2 Sv) is concomitant to a significant increase in incoming and outgoing lateral
458 Cant fluxes (74%), as well as in regional air-sea Cant fluxes (70%) and Cant storage rate (70% to
459 77%). The high (85-97) to low (2002-06) NAO transition phase is nevertheless characterized by a
460 rather homogeneous yet not significant decrease in MOC magnitude at 36° N (11.8 ± 0.2 Sv to
461 11.7 ± 0.2 Sv) and across the OVIDE section (13.3 ± 0.2 Sv to 12.9 ± 0.2 Sv). South of the OVIDE
462 section, this is concomitant to a progressive and significant intensification by 29% in northward
463 transport of Cant at 36° N and 8% in air-sea Cant fluxes. North of the OVIDE section, the high to
464 low NAO transition phase coincides with an average increase by 15% in incoming and outgoing
465 Cant fluxes (transport and gas exchange), in opposition to results by Pérez et al. (2013). The large
466 interannual variability of these fluxes revealed by Figs. 8 and S3 highlighted the significant role
467 played by the time window size on the trend evaluation (e.g. consider trend between 1990-91 and
468 1999-2000 in the model at the OVIDE section) that could explain differences observed with Pérez
469 et al. (2013). The increase in Cant fluxes for each box is, however, not as large over the 16-year
470 period (1985-2006, from strong to low NAO) compared to 1967-1997 (from low to strong NAO)
471 (+70-72%) and lead to an increase in regional Cant budget of 13% (south) to 19% (north).

472 Moreover, statistical analysis of each individual NAO period shows that the regional Cant storage
473 rate is strongly correlated with the air sea Cant fluxes during the strong NAO phase (85-97, South: r
474 = 0.94, p-value = 0.00, $r^2 = 0.88$; North : $r = 0.97$, p-value = 0.00, $r^2 = 94$; table 3, hatched arrows
475 on Fig. 10), consistent with the strong ventilation observed during this period (e.g. Sarafanov,
476 2009). It is nevertheless related to Cant transport divergence (incoming – outgoing Cant transport)
477 during the low NAO phase (67-77: South: $r = 0.81$, p-value = 0.00, $r^2 = 0.66$; North : $r = 0.99$ p-
478 value = 0.05, $r^2 = 98$; 2002-06 : South: $r = 0.96$, p-value = 0.01, $r^2 = 0.92$; North : $r = 0.93$, p-value
479 = 0.02, $r^2 = 0.87$; table 3), consistent with result from section III. Although the transport divergence
480 of Cant explains more than 70% of the interannual variability of the regional Cant storage rate over



481 these two low NAO periods with low atmospheric forcing, its longer-term mean values close to zero
482 (67-77; 85-97; 2002-06) cannot explain those of Cant inventory in the subpolar North Atlantic
483 region (Fig. 10). Over the period 1964-2006, the Cant storage rate is in fact strongly correlated to
484 the air to sea anthropogenic CO₂ exchange (south : $r = 0.92$, $p\text{-value} = 0.00$; north : $r = 0.77$, $p\text{-value}$
485 $= 0.00$, table 3), as opposed to the transport divergence recorded in both region (1964 to 2006, south
486 : $r = -0.53$, $p\text{-value} = 0.00$; north : $r^2 = 0.34$, $p\text{-value} = 0.02$). The long term change in air-sea Cant
487 fluxes explains thus 59% (north) to 84% (south) of the multi decadal variability of Subpolar North
488 Atlantic Cant inventory. As the anthropogenic CO₂ concentration increase in the atmosphere, the
489 North Atlantic Cant inventory increase substantially.

490

491

492 To conclude, although the interannual variability of Cant storage rate in the Subpolar North Atlantic
493 region is controlled by the northward advective transport divergence during the low NAO phase, its
494 long term change is driven by air to sea anthropogenic CO₂ exchange over the period 1964-2006.
495 Moreover, the northward advective transport of Cant, modulated by the MOC intensity, seems to be
496 also controlled by the increasing Cant concentration in the upper limb of MOC through
497 preconditioning in the subtropical region. Our model analysis suggests that assuming unabated
498 emissions of CO₂, the storage rate of Cant in the Subpolar North Atlantic is expected to increase
499 assuming MOC fluctuations within observed boundaries. However, under a future strong decrease
500 in MOC in response to global warming (IPCC projection 25%, Collins et al., 2013) the storage rate
501 might nevertheless decrease.

502

503 **References**

- 504 Álvarez, M., Pérez, F. F., Bryden, H., & Ríos, A. F. : Physical and biogeochemical transports
505 structure in the North Atlantic subpolar gyre, *J Geophys Res: Oceans*, 109(C3), 2004.
- 506 Aumont, O., and Bopp, L.: Globalizing results from ocean in situ iron fertilization studies, *Global*
507 *Biogeochem Cy*, 20(2), 2006.
- 508 Barnier, B., Madec, G., Penduff, T., Molines, J. M., Treguier, A. M., Le Sommer, J., Beckmann, A.,
509 Biastoch, A., Böning, C., Dengg, J., Derval, C., Durand, E., Gulev, S., Remy, E., Talandier, C.,
510 Theetten, S., Maltrud, M., McClean, J., and De Cuevas, B.: Impact of partial steps and
511 momentum advection schemes in a global ocean circulation model at eddy-permitting
512 resolution, *Ocean Dynam.*, 56, 543–567, 2006
- 513 Bourgeois, T., Orr, J. C., Resplandy, L., Terhaar, J., Ethé, C., Gehlen, M., and Bopp, L.: Coastal-
514 ocean uptake of anthropogenic carbon, *Biogeosciences* 13, 4167-4185, doi:10.5194/bg-13-4167-



- 515 2016, 2016.
- 516 Brodeau, L., Barnier, B., Treguier, A. M., Penduff, T. and Gulev, S.: An ERA40-based atmospheric
517 forcing for global ocean circulation models, *Ocean Modelling*, 31(3), 88-104, 2010.
- 518 Bryden, H. L. and Imawaki, S.: Ocean heat transport, *International Geophysics Series*, 77, 455-474,
519 2001.
- 520 Bryden, H. L., Longworth, H. R. and Cunningham, S. A.: Slowing of the Atlantic meridional
521 overturning circulation at 25 N, *Nature*, 438(7068), 655-657, 2005.
- 522 Ciais, P., Sabine, C., Bala, G., Bopp, L., Brovkin, V., Canadell, J., Chhabra, A., Defries, R.,
523 Galloway, J., Heimann, M., Jones, C., Le Quéré, C., Myneni, R.B., Piao, S and Thornton, P.:
524 Carbon and other biogeochemical cycles. In: *Climate Change 2013: The Physical Science Basis.*
525 *Contribution of Working Group I to the Fifth Assessment Report of the Intergovernmental Panel*
526 *on Climate Change* [Stocker, T.F., D. Qin, G-K. Plattner, M. Tignor, S.K. Allen, J. Boschung, A.
527 Nauels, Y. Xia, V. Bex and P.M. Midgley (eds.)]. Cambridge University Press, Cambridge,
528 United Kingdom and New York, NY, USA, 2013.
- 529 Collins, M., Knutti, R., Arblaster, J., Dufresne, J-L., Fichet, T., Friedlingstein, P., Gao, X.,
530 Gutwoski, W.J., Johns, T., Krinner, G., Shongwe, M., Tebaldi, C., Weaver, A.J. and Wehner, M.:
531 Long-term Climate Change: Projections, Commitments and Irreversibility. . In: *Climate Change*
532 *2013: The Physical Science Basis. Contribution of Working Group I to the Fifth Assessment*
533 *Report of the Intergovernmental Panel on Climate Change* [Stocker, T.F., D. Qin, G-K. Plattner,
534 M. Tignor, S.K. Allen, J. Boschung, A. Nauels, Y. Xia, V. Bex and P.M. Midgley (eds.)].
535 Cambridge University Press, Cambridge, United Kingdom and New York, NY, USA, 2013.
- 536 Conkright, M. E., Locarnini, R. A., Garcia, H. E., O'Brien, T. D., Boyer, T. P., Stephens, C. and
537 Antonov, J. I.: *World Ocean Database 2001: Objective analyses, data statistics and figures*, 2002
- 538 Crueger, T., Roeckner, E., Raddatz, T., Schnur, R. and Wetzol, P.: Ocean dynamics determine the
539 response of oceanic CO₂ uptake to climate change, *Clim dynam*, 31(2-3), 151-168, 2008.
- 540 Curry, R. G. and McCartney, M. S.: Ocean gyre circulation changes associated with the North
541 Atlantic Oscillation, *J Phys Oceanogr*, 31(12), 3374-3400, 2001.
- 542 Daniault, N., Mercier, H., Lherminier, P., Sarafanov, A., Falina, A., Zunino Rodriguez, P., Pérez,
543 F.F., Rios, A.F., Ferron, B., Huck, T., Thierry, V. and Gladyshev, S.: The northern North Atlantic
544 Ocean mean circulation in the early 21st century. *Prog Oceanogr*, 146, 142-158.
545 <http://dx.doi.org/10.1016/j.pocean.2016.06.007>, 2016.
- 546 de Boissésou, E., Thiery, V., Mercier, H., Caniaux, G and Débruyères, D. : Origin, formation and
547 variability of the Subpolar Mode Water located over the Reykjanes Ridge. *JGR (C12005)*, 117,
548 doi: 10.1029/2011JC007519, 2012



- 549 Dee, D. P., Uppala, S. M., Simmons, A. J., Berrisford, P., Poli, P., Kobayashi, S., Andrae, U.,
 550 Balmaseda, M. A., Balsamo, G., Bauer, P., Bechtold, P., Beljaars, A. C. M., van de Berg, L.,
 551 Bidlot, J., Bormann, N., Delsol, C., Dragani, R., Fuentes, M., Geer, A. J., Haimberger, L., Healy,
 552 S. B., Hersbach, H., Hólm, E. V., Isaksen, I., Kållberg, P., Köhler, M., Matricardi, M., McNally,
 553 A. P., Monge-Sanz, B. M., Morcrette, J.-J., Park, B.-k., Peubey, C., de Rosnay, P., Tavolato, C.,
 554 Thépaut, J.-N and Vitart, F.: The ERA-Interim reanalysis: configuration and performance of the
 555 data assimilation system, *Q. J. Roy. Meteor. Soc.* 137 (656), 553-597, 2011
- 556 Delworth, T. L. and Zeng, F.: The impact of the North Atlantic Oscillation on climate through its
 557 influence on the Atlantic Meridional Overturning Circulation, *J Climate*, 2015.
- 558 Desbruyères, D., Thierry, V. and Mercier, H.: Simulated decadal variability of the meridional
 559 overturning circulation across the A25-OVIDE section, *JGR* 118(1), 462-475, doi:
 560 10.1029/2012JC008342, 2013
- 561 Dickson, R., Lazier, J., Meincke, J. and Rhines, P.: Long-term coordinated changes in the
 562 convective activity of the North Atlantic. In *Decadal Climate Variability* (pp. 211-261). Springer
 563 Berlin Heidelberg, 1996.
- 564 García-Ibáñez, M. I, Pardo, P. C., Carracedo, L., Mercier, H., Lherminier, P., Rios, A. F. and Pérez,
 565 F. F.: Structure, transports and transformations of the water masses in the Atlantic Subpolar Gyre,
 566 *Prog. Oceanogr.* 135, 18-36, <http://dx.doi.org/10.1016/j.pocean.2015.03.009>, 2015
- 567 Gent, P. R., and McWilliams, J. C.: Isopycnal mixing in ocean circulation models, *J Phys Oceanogr*,
 568 20(1), 150-155, 1990.
- 569 Gruber, N., Gloor, M., Mikaloff Fletcher, S. E., Doney, S. C., Dutkiewicz, S., Follows, M.
 570 J., Gerber, M., Jacobson, A.R., Joos, F., Lindsay, K., Menemenlis, D., Mouchet, A., Muller, S.A,
 571 Sarmiento, J.L. and Takahashi, T.: Oceanic sources, sinks, and transport of atmospheric CO₂,
 572 *Global Biogeochem Cy*, 23(1), 2009.
- 573 Häkkinen, S., and Rhines, P. B.: Decline of subpolar North Atlantic circulation during the 1990s,
 574 *Science*, 304(5670), 555-559, 2004.
- 575 Harvey, J.: Theta-S relationships and water masses in the eastern North Atlantic, *Deep Sea Res* 29
 576 (8), 1021–1033, [http://dx.doi.org/10.1016/0198-0149\(82\)90025-5](http://dx.doi.org/10.1016/0198-0149(82)90025-5), 1982.
- 577 Hurrell, J. W.: Decadal trends in the North Atlantic Oscillation: regional temperatures and
 578 precipitation, *Science*, 269(5224), 676-679, 1995.
- 579 Osborn, T.J.: Recent variations in the winter North Atlantic Oscillation, *Weather* **61**, 353-355, 2006.
- 580 Osborn, T.J.: Winter 2009/2010 temperatures and a record-breaking North Atlantic Oscillation
 581 index, *Weather* **66**, 19-21, 2011.
- 582 IOC, SCOR and IAPSO: The international thermodynamic equation of seawater - 2010: Calculation



- 583 and use of thermodynamic properties. Intergovernmental Oceanographic Commission, Manuals
584 and Guides No. 56, UNESCO (English), 196 pp. Available from <http://www.TEOS-10.org>. See
585 section 3.3 of this TEOS-10 Manual, 2010.
- 586 Key, R. M., Kozyr, A., Sabine, C. L., Lee, K., Wanninkhof, R., Bullister, J. L., Feely, R. A., Millero,
587 F. J., Mordy, C. and Peng, T.-H.: A global ocean carbon climatology: Results from Global Data
588 Analysis Project (GLODAP), Global Biogeochem Cy 18, GB4031, doi:10.1029/2004GB002247,
589 2004
- 590 Khatiwala, S., Tanhua, T., Fletcher, S. M., Gerber, M., Doney, S. C., Graven, H. D., Gruber, N.,
591 McKinley, G.A., Murata, A., Rios, A.F., and Sabine, C. L.: Global ocean storage of
592 anthropogenic carbon, *Biogeosciences*, 10(4), 2169-2191, 2013.
- 593 Körtzinger, A., Rhein, M., and Mintrop, L.: Anthropogenic CO₂ and CFCs in the North Atlantic
594 Ocean-A comparison of man-made tracers, *Geophys Res Lett*, 26(14), 2065-2068, 1999.
- 595 Lazier, J., Hendry, R., Clarke, A., Yashayaev, I. and Rhines, P.: Convection and restratification in
596 the Labrador Sea, 1990–2000, *Deep Sea Res PtI*, 49(10), 1819-1835, 2002.
- 597 Le Quéré, C., Raupach, M. R., Canadell, J. G., Marland, G. and co-authors: Trends in the sources
598 and sinks of carbon dioxide, *Nature Geosciences*, 2(12), 831-836, 2009.
- 599 Le Quéré, C., Peters, G. P., Andres, R. J., Andrew, R. M., and co-authors : Global carbon budget
600 2013, *ESSD*, 6, 235–263, doi:10.5194/essd-6-235-2014, 2014.
- 601 Le Quéré, C. Moriarty, R., Andrew, R.M., Peters, G.P., and co-authors: Global Carbon Budget
602 2014, 2015.
- 603 Lherminier, P., Mercier, H., Gourcuff, C., Alvarez, M., Bacon, S. and Kermabon, C.: Transports
604 across the 2002 Greenland-Portugal Ovide section and comparison with 1997, *J Geophys Res-*
605 *Oceans*, 112(C7), 2007.
- 606 Lherminier, P., Mercier, H., Huck, T., Gourcuff, C., Perez, F. F., Morin, P., Sarafanov, A.,
607 and Falina, A.: The Atlantic Meridional Overturning Circulation and the subpolar gyre observed
608 at the A25-OVIDE section in June 2002 and 2004, *Deep Sea Res Pt I* 57(11), 1374-1391, 2010.
- 609 Madec, G., and Imbard, M.: A global ocean mesh to overcome the North Pole singularity, *Climate*
610 *Dy* 12(6), 381-388, 1996.
- 611 Madec, G.: NEMO Ocean Engine, vol. 27, pp. 1–217, Note du Pole de modélisation de l’Institut
612 Pierre-Simon Laplace, France, 2008
- 613 Marsh, R., De Cuevas, B. A., Coward, A. C., Bryden, H. L., and Álvarez, M.: Thermohaline
614 circulation at three key sections in the North Atlantic over 1985–2002, *Geophys Res Lett* 32(10),
615 2005
- 616 McKinley, G.A., Pilcher, D.J., Fay, A.R., Lindsay, K., Long, M.C. and Lovenduski, N.S.:



- 617 Timescales for detection of trends in the ocean carbon sink. *Nature*, 530, 469-472, 2013.
- 618 Mercier, H., Lherminier, P., Sarafanov, A., Gaillard, F., Danialt, N., Desbruyères, D., Falina, A.,
619 Ferron, B., Gourcuff, C., Huck, T. and Thierry, V.: Variability of the meridional overturning
620 circulation at the Greenland–Portugal OVIDE section from 1993 to 2010, *Prog Oceanogr* 132
621 (2015) 250–261, [doi:10.1016/j.pocean.2013.11.001](https://doi.org/10.1016/j.pocean.2013.11.001), 2015
- 622 Mikaloff Fletcher, S. E., Gruber, N., and Jacobson, A. R.: Ocean Inversion Project How-to
623 Document Version 1.0, 18 pp. Institute for Geophysics and Planetary Physics, University of
624 California, Los Angeles, 2003
- 625 Mikaloff Fletcher, S. E., Gruber, N., Jacobson, A. R., Doney, S. C., Dutkiewicz, S., Gerber, M.,
626 Follows, M., Joos, F., Lindsay, K., Menemenlis, D., Mouchet, A., Müller, S.A. and Sarmiento,
627 J.L.: Inverse estimates of anthropogenic CO₂ uptake, transport, and storage by the ocean. *Global*
628 *Biogeochem Cy* 20(2), doi:10.1029/2005GB002530, 2006.
- 629 Pérez, F. F., Vázquez-Rodríguez, M., Louarn, E., Padín, X. A., Mercier, H., and Ríos, A. F. :
630 Temporal variability of the anthropogenic CO₂ storage in the Irminger Sea, *Biogeosciences*,
631 5(6), 1669-1679, 2008
- 632 Pérez, F. F., Vázquez Rodríguez, M., Mercier, H., Velo, A., Lherminier, P. and Ríos, A. F. : Trends
633 of anthropogenic CO₂ storage in North Atlantic water masses, *Biogeosciences*, 7, 1789–1807,
634 doi:10.5194/bg-7-1789-2010, 2010.
- 635 Pérez, F. F., Mercier, H., Vázquez-Rodríguez, M., Lherminier, P., Velo, A., Pardo, P. C., Roson,
636 G., and Ríos, A. F. : Atlantic Ocean CO₂ uptake reduced by weakening of the meridional
637 overturning circulation, *Nature Geoscience*, 6(2), 146-152, doi: 10.1038/NGEO1680, 2013
- 638 Pickart, R. S., Straneo, F. and Moore, G. W. K.: Is Labrador sea water formed in the Irminger
639 basin?, *Deep Sea Res Pt I* 50(1), 23-52, 2003.
- 640 Pickart, R. S., Torres, D. J. and Fratantoni, P. S.: The East Greenland Spill Jet. *J Phys Oceanogr*
641 35(6), 1037-1053, 2005.
- 642 Pollard, R.T., Griffiths, M.J., Cunningham, S.A., Read, J.F., Perez, F.F. and Rios, A.F.: Vivaldi
643 1991 – a study of the formation, circulation and ventilation of Eastern North Atlantic Central
644 Water, *Prog Oceanogr* 37, 167–192. [http://dx.doi.org/10.1016/S0079-6611\(96\)00008-0](http://dx.doi.org/10.1016/S0079-6611(96)00008-0), 1996.
- 645 Rhein, M., Fischer, J., Smethie, W. M., Smythe-Wright, D., Weiss, R. F., Mertens, C., Min, D.H.,
646 Fleischmann, U., and Putzka, A.: Labrador Sea Water: Pathways, CFC inventory, and formation
647 rates, *J Phys Oceanogr* 32(2), 648-665, 2002.
- 648 Rhein, M., Kieke, D., Hüttl-Kabus, S., Roessler, A., Mertens, C., Meissner, R., Klein, B., Böning,
649 C.W. and Yashayaev, I.: Deep water formation, the subpolar gyre, and the meridional
650 overturning circulation in the subpolar North Atlantic, *Deep-Sea Res Pt II* 58(17), 1819-1832,



- 651 2011.
- 652 Sabine, C. L., Feely, R. A., Gruber, N., Key, R. M., Lee, K., Bullister, J. L., Wanninkhof, R.,
653 Wong, C.S., Wallace, D.W.R., Tilbrook, B., Millero, F.J., Peng, T-H., Kozyr, A., Ono, T. and
654 Ríos, A.F.: The oceanic sink for anthropogenic CO₂. *Science* 305(5682), 367-371, 2004.
- 655 Sarafanov, A.: On the effect of the North Atlantic Oscillation on temperature and salinity of the
656 subpolar North Atlantic intermediate and deep waters. *ICES Journal of Marine Science: Journal*
657 *du Conseil*, 66(7), 1448-1454, 2009.
- 658 Sférian, R., Ribes, A. and Bopp, L.: Detecting the anthropogenic influences on recent changes in
659 ocean carbon uptake: *Geophys. Res. Lett.*, 41, 5968-5977, 2014
- 660 Steinfeldt, R., Rhein, M., Bullister, J. L. and Tanhua, T.: Inventory changes in anthropogenic
661 carbon from 1997–2003 in the Atlantic Ocean between 20 S and 65 N, *Global Biogeochem Cy*
662 23(3), 2009.
- 663 Tanhua, T., Olsson, K. A. and Jeansson, E.: Formation of Denmark Strait overflow water and its
664 hydro-chemical composition, *J Mar Sys* 57(3), 264-288, 2005.
- 665 Timmermann, R., Goosse, H., Madec, G., Fichefet, T., Ethe, C. and Duliere, V.: On the
666 representation of high latitude processes in the ORCA-LIM global coupled sea ice–ocean model.
667 *Ocean Modelling*, 8(1), 175-201, 2005.
- 668 Treguier, A-M., Gourcuff, C., Lherminier, P., Mercier, H., Barnier, B., Madec, G., Molines, J-M.,
669 Penduff, T., Czeschel, L., Böning, C.W.: Internal and Forced variability along a section between
670 Greenland and Portugal in the CLIPPER Atlantic model. *Ocean Dynam* 56 (5-6), 568-580,
671 doi:10.1007/s10236-006-0069-y, 2006
- 672 Tsuchiya, M., Talley, L.D., McCartney, M.S.: An eastern Atlantic section from Iceland southward
673 across the equator. *Deep Sea Res Pt A* 39 (11), 1885–1917. [http://dx.doi.org/10.1016/0198-](http://dx.doi.org/10.1016/0198-0149(92)90004-D)
674 [0149\(92\)90004-D](http://dx.doi.org/10.1016/0198-0149(92)90004-D), 1992
- 675 Våge, K., Pickart, R. S., Sarafanov, A., Knutsen, Ø., Mercier, H., Lherminier, P., van Aken, H.M.,
676 Meincke, J., Quadfasel, D. and Bacon, S.: The Irminger Gyre: Circulation, convection, and
677 interannual variability, *Deep-Sea Res Pt I* 58(5), 590-614, doi:10.1016/j.dsr.2011.03.001, 2011.
- 678 van Aken, H.M. and Becker, G.: Hydrography and through-flow in the northeastern North Atlantic
679 Ocean: the NANSEN project, *Prog Oceanogr* 38 (4), 297–346, [http://dx.doi.org/10.1016/S0079-](http://dx.doi.org/10.1016/S0079-6611(97)00005-0)
680 [6611\(97\)00005-0](http://dx.doi.org/10.1016/S0079-6611(97)00005-0), 1996
- 681 van Aken, H. M. : The hydrography of the mid-latitude northeast Atlantic Ocean: I: The deep water
682 masses, *Deep-Sea ResPt I* 47(5), 757-788, 2000.
- 683 Vázquez-Rodríguez, M., Padin, X. A., Ríos, A. F., Bellerby, R. G. J. and Pérez, F. F.: An upgraded
684 carbon-based method to estimate the anthropogenic fraction of dissolved CO₂ in the Atlantic



- 685 Ocean, *Biogeosciences Discuss.*, 6, 4527–4571, doi:10.5194/bgd-6-4527-2009, 2009.
- 686 Velo, A., Pérez, F. F., Lin, X., Key, R. M., Tanhua, T., de la Paz, M., Olsen, A., van Heuven, S.,
687 Jutterström, S. and Ríos, A. F.: CARINA data synthesis project: pH data scale unification and
688 cruise adjustments, *Earth Syst. Sci. Data*, 2, 133–155, doi:10.5194/essd-2-133-2010, 2010.
- 689 Wanninkhof, R.: Relationship between wind speed and gas exchange over the ocean, *Jeophys Res*
690 97(C5), 7373–7382, 1992.
- 691 Wanninkhof, R., Park, G.H., Takahashi, T., Sweeney, C., Feely, R.A., Nojiri, Y., Gruber, N.,
692 Doney, S.C., McKinley, G.A., Lenton, A., Le Quere, C., Heinze, C. Schwinger, J., Graven, H.,
693 and Khatiwala, S.: Global Ocean carbon uptake: Magnitude, variability and trend,
694 *Biogeosciences* 10, 1983–2000, doi:10.5194/bg-10-1983-2013, 2013
- 695 Yashayaev, I.: Hydrographic changes in the Labrador Sea, 1960–2005, *Prog Oceanogr* 73(3), 242–
696 276, 2007.
- 697 Yashayaev, I. and Dickson, B.: Transformation and fate of overflows in the northern North Atlantic.
698 In *Arctic–Subarctic Ocean Fluxes* (pp. 505–526). Springer Netherlands, 2008.
- 699 Zunino, P., Garcia-Ibanez, M. I., Lherminier, P., Mercier, H., Ríos, A. F. and Pérez, F. F.:
700 Variability of the transport of anthropogenic CO₂ at the Greenland-Portugal OVIDE section:
701 Controlling mechanisms, *Biogeosciences*, 11, 2375–2389, doi:10.5194/bg-11-2375-2014, 2014
- 702 Zunino, P., Lherminier, P., Mercier, H., Padín, X. A., Ríos, A. F. and Pérez, F. F.: Dissolved
703 inorganic carbon budgets in the eastern subpolar North Atlantic in the 2000s from in situ data,
704 *Geophys Res Lett* 42(22), 9853–9861, 2015.
- 705 Zunino, P., Pérez, F. F., Fajar, N. M., Guallart, E. F., Ríos, A. F., Pelegrí, J. L. and
706 Hernández-Guerra, A.: Transports and budgets of anthropogenic CO₂ in the tropical North
707 Atlantic in 1992–1993 and 2010–2011, *Global Biogeochem Cy*, 29(7), 1075–1091, 2015.

708

709 **Acknowledgment**

710 For this work, VR was funded through the EU FP7 project CARBOCHANGE (grant 264879).
711 Simulations were made using HPC resources from GENCI-IDRIS (grant x2015010040). We are
712 grateful to Christian Ethe, who largely contributed to obtain Cant transport in online over the period
713 2003–2011. We want to acknowledge HM (supported by CNRS and the ATLANTOS H2020 project
714 (GA 633211)) and colleagues for leading OVIDE project (supported by French research institutions,
715 IFREMER and CNRS/INSU).

716

717 **Table captures**

718 Table 1: OVIDE cruises



OVIDE name	Month/year	Vessel	Reference	CARINA expocode
OVIDE 2002	06-07/2002	N/O Thalassa	Lherminier et al., 2007	35TH20020611
OVIDE 2004	06-07/2004	N/O Thalassa	Lherminier et al., 2010	35TH20040604
OVIDE 2006	05-06/2006	R/V Maria S. Merian	Gourcuff et al., 2011	06MM20060523
OVIDE 2008	06-07/2008	N/O Thalassa	Mercier et al. 2015	35TH20080610
OVIDE 2010	06-07/2010	N/O Thalassa	Mercier et al., 2015	35TH20100608

719

720 **Table 2:** Model-data comparison over the period covered by OVIDE cruises (2002-2010). Average
 721 and standard deviation (SD) for observation-based estimates (column 2) and model output (columns
 722 3 to 5). Model output: (1) June average with SD being a measure of interannual variability, (2)
 723 average year with SD corresponding to the average seasonal variability, or (3) average over the full
 724 period with SD being representative of total variability (interannual + seasonal).

	OVIDE data set	ORCA05-PISCES		
		June only	average year	full period
Mass transport (sv)	0.74±0.75	0.19±0.33	0.67±0.24	0.67±0.46
MOC σ (sv)	15.5±2.3	13.4±0.6	12.7±0.6	13.4±2.43
σ MOC (kg m ⁻³)	32.14	32.02±0.05	31.95±0.04	31.98±0.12
[Cant] _{section} (μ mol kg ⁻¹)	25.4±1.8	18.4±1.1	18.4±1.1	18.4±1.1
[Cant] _{upper} (μ mol kg ⁻¹)	45.2±3.0	38.9±3.0	39.4±3.0	39.4±3.0
[Cant] _{lower} (μ mol kg ⁻¹)	19.4±1.6	14.8±1.0	14.9±1.0	14.9±1.0
Δ [Cant ^{up-low}] (μ mol kg ⁻¹)	25.8±1.4	24.1±1.6	24.6±1.6	24.5±2.2

725

726 **Table 3:** Correlation coefficient (r), p-value and coefficient of determination (r²) between the time
 727 rate of change (Trate), the divergence of Cant transport (DTcant) and air sea Cant fluxes (Fcant) for
 728 the three boxes. DTcant = incoming – outgoing Cant fluxes across the boundaries of boxes.

Box 25° N to OVIDE section	
2003-11	Trate/DTcant : r = 0.96, p-value = 0.00, r ² = 0.93 Trate/Fcant : r = - 0.54, p-value = 0.00, r ² = 0.30
Box OVIDE section to Nordic sills	
2003-11	Trate/DTcant : r = 0.95, p-value = 0.00, r ² = 0.89 Trate/Fcant : r = - 0.71, p-value = 0.00, r ² = 0.51
Box 36° N to OVIDE section	
1967-77	Trate/DTcant : r = 0.81, p-value = 0.00, r ² = 0.66 Trate/Fcant : r = - 0.66, p-value = 0.02, r ² = 0.45
1985-97	Trate/DTcant : r = -0.65, p-value = 0.02, r ² = 0.42 Trate/Fcant : r = 0.94, p-value = 0.00, r ² = 0.88
2002-06	Trate/DTcant : r = 0.96, p-value = 0.01, r ² = 0.92 Trate/Fcant : r = 0.61, p-value = 0.27, r ² = 0.37
1964-06	Trate/DTcant : r = -0.53, p-value = 0.00, r ² = 0.28 Trate/Fcant : r = 0.92, p-value = 0.00, r ² = 0.84



Box OVIDE section to Nordic sills	
1967-77	Trate/DTcant : $r = 0.99$, $p\text{-value} = 0.05$, $r^2 = 0.98$
	Trate/Fcant : $r = -0.22$, $p\text{-value} = 0.05$, $r^2 = 0.05$
1985-97	Trate/DTcant : $r = 0.87$, $p\text{-value} = 0.00$, $r^2 = 0.74$
	Trate/Fcant : $r = 0.97$, $p\text{-value} = 0.00$, $r^2 = 0.94$
2002-06	Trate/DTcant : $r = 0.93$, $p\text{-value} = 0.02$, $r^2 = 0.87$
	Trate/Fcant : $r = 0.60$, $p\text{-value} = 0.28$, $r^2 = 0.36$
1964-06	Trate/Dtcant : $r = 0.34$, $p\text{-value} = 0.02$, $r^2 = 0.12$
	Trate/Fcant : $r = 0.77$, $p\text{-value} = 0.00$, $r^2 = 0.59$

729

730

731 **Figures captions**

732 Fig. 1: Year 2010 column inventory (molC m^{-2}) of anthropogenic Carbon: (a) model output and (b)
 733 after Khatiwala et al. [2009].

734

735 Fig. 2: Year 2010 North Atlantic column inventory (molC m^{-2}) of anthropogenic Carbon: model
 736 output from 25°N to Greenland-Iceland-Scotland sills. The OVIDE cruise track between Greenland
 737 and Portugal is indicated by the continuous line.

738

739 Fig. 3: Water column distribution of (a-b) salinity, (c-d) dissolved oxygen ($\mu\text{mol kg}^{-1}$) and (e-f)
 740 dissolved silica ($\mu\text{mol kg}^{-1}$) along the Greenland-Portugal OVIDE section in June 2002: model
 741 output (left) and sampled during the OVIDE cruise (right). Water masses and currents cited in
 742 section III.1 are identified on the right panel: East North Atlantic Central Water (ENACW),
 743 Mediterranean Water (MW), Labrador Sea Water (LSW), lower North-East Atlantic Deep Water
 744 (NEADW) and Eastern Reykjanes Ridge Current (ERRC). Four basins are delimited by grey
 745 dashed vertical lines. From Greenland to the coast of Portugal: Irminger basin (IrB), Iceland basin
 746 (IcB), East – North Atlantic basin (ENAB) and Iberian Basin (IbB).

747

748 Fig. 4. Monthly evolution of the net volume transported across the Greenland-Portugal OVIDE
 749 section (S_v): model output (black continuous lines) and estimates derived from the OVIDE data set
 750 (orange dots) over the period 2002-2010

751

752 Fig. 5. Vertically integrated cumulative mass transport (S_v): model output for the month of June
 753 over the period 2002-10 (continuous line for mean value; shadows for confidence interval) (a) from
 754 bottom to each specific density level (σ_1 with 0.01 kg m^{-3} resolution), note that the sign of the
 755 profile has been changed, and (b) from Greenland to Portugal (km) compared to estimates derived



756 from OVIDE (dashed lines). On panel (a) the black horizontal lines indicate the density of $MOC\sigma$
757 maximum corresponding to the separation between the upper (red) and lower (blue) limbs of MOC,
758 in the model ($\sigma_{MOC} = 32.02 \pm 0.05 \text{ kg m}^{-3}$, black continuous line) and observation-based assessments
759 ($\sigma_{MOC} = 32.14 \text{ kg m}^{-3}$, Zunino et al., 2014; black dashed line). On panel (b) the position of the
760 Western and Eastern NAC branches as well as the Irminger current, a NAC modified branch, are
761 indicated in grey (Mercier et al., 2015).

762

763 Fig. 6 : Water column distribution of anthropogenic C concentrations ($\mu\text{mol kg}^{-1}$) along the
764 Greenland-Portugal OVIDE section in June 2002: (a) model output and (b) as estimated from the
765 OVIDE data set. The difference between these both assessments (model – OVIDE) over the OVIDE
766 period (June 2002-04-06-08-10) and its standard deviation are displayed on Fig. c and d. Grey
767 dashed lines delimit the four basins identified on Fig. 3. Black continuous and dashed lines indicate
768 the limit between the upper and the lower limbs of the MOC in the model and the OVIDE data set.

769

770 Fig. 7: Anthropogenic C budget of the Subtropical and Subpolar North Atlantic regions over the
771 period 2003-2011. Average values and their standard deviation were estimated from smoothed time
772 series. The horizontal arrows show the lateral Cant transport in PgC yr^{-1} (black font). Red numbers
773 in the panel indicate the Cant storage rate in PgC yr^{-1} . The vertical arrows show the anthropogenic
774 air-sea CO_2 fluxes in PgC yr^{-1} . Green numbers represent the heat transport across sections in PW.
775 Boundaries and surface area (m^2) of each box are indicated below the panels.

776

777 Fig. 8: Simulated annual time series of MOC magnitude ($MOC\sigma$, Sv) and transport of heat (PW)
778 and anthropogenic C (PgC yr^{-1}) at 36°N and at the OVIDE section estimated over the period 1958-
779 2012.

780

781 Fig. 9: Simulated annual time series of $MOC\sigma$ anomaly over the period 1958-2012 along the
782 Greenland-Portugal OVIDE section. Three particular periods are highlighted by grey areas: 1967-
783 77 characterized by a weak $MOC\sigma$ (negative $MOC\sigma$ anomaly), 1985-97 with a strong $MOC\sigma$
784 (positive $MOC\sigma$ anomaly) and since 2002 (negative trend in $MOC\sigma$).

785

786 Fig. 10: Anthropogenic C budget for the period 1967-1977 (weak $MOC\sigma$), 1985-1997 (strong
787 $MOC\sigma$) and 2002-2006 ($MOC\sigma$ negative trend) in the Subpolar North Atlantic region defined from
788 36°N to Nordic sill and divided in two boxes by the OVIDE section. Average values and their
789 standard deviation were estimated from smoothed times series (Fig. S3). Vertical arrows show the



790 air to sea anthropogenic CO₂ fluxes in PgC yr⁻¹, black horizontal arrows correspond to the advective
791 transport of Cant across section in PgC yr⁻¹. Red numbers indicate the Cant storage rate in each box.
792 The size of arrows and fonts used for the storage rate are proportional to the 2002-2006 budget.
793 Hatched arrows indicate a strong correlation between the term and the regional Cant storage rate
794 over the period of interest.
795
796

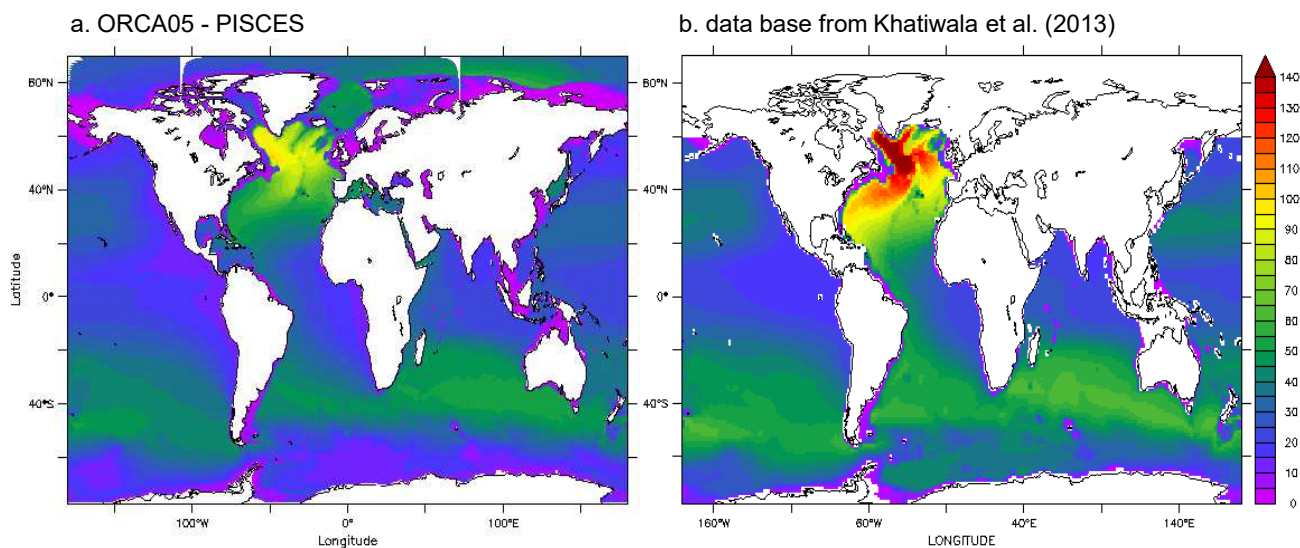


Fig. 1: Year 2010 column inventory (molC m^{-2}) of anthropogenic Carbon: (a) model output and (b) after Khatiwala et al. [2009].

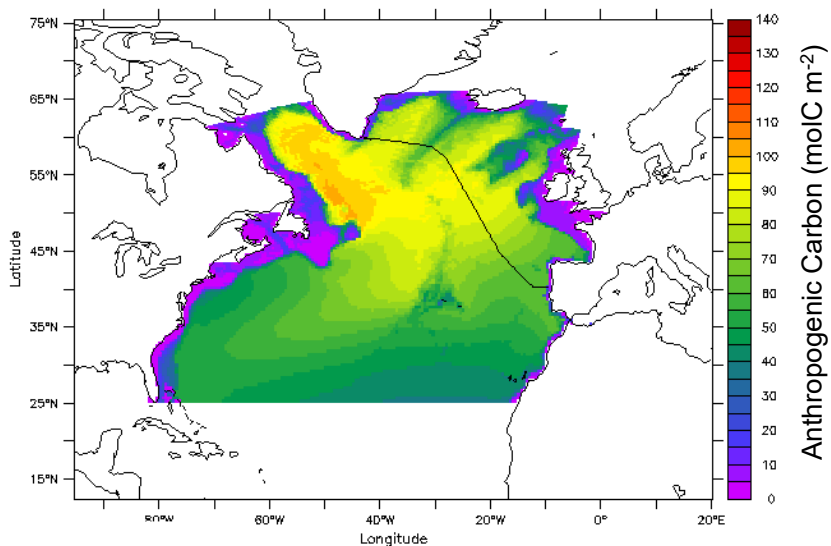


Fig. 2: Year 2010 North Atlantic column inventory (molC m^{-2}) of anthropogenic Carbon: model output from 25°N to Greenland-Iceland-Scotland sills. The OVIDE cruise track between Greenland and Portugal is indicated by the continuous line.

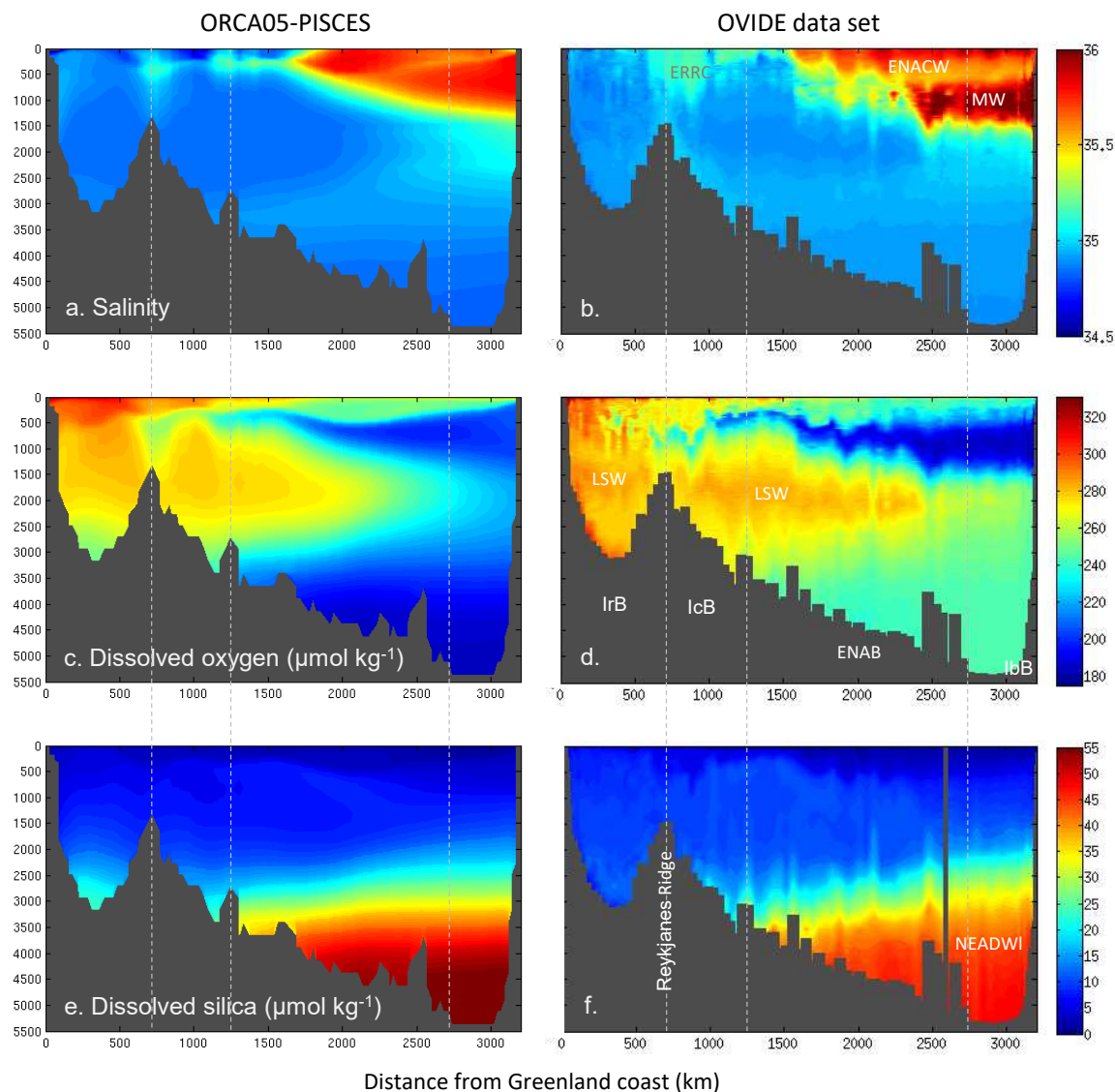


Fig. 3: Water column distribution of (a-b) salinity, (c-d) dissolved oxygen ($\mu\text{mol kg}^{-1}$) and (e-f) dissolved silica ($\mu\text{mol kg}^{-1}$) along the Greenland-Portugal OVIDE section in June 2002: model output (left) and sampled during the OVIDE cruise (right). Water masses and currents cited in section III.1 are identified on the right panel: East North Atlantic Central Water (ENACW), Mediterranean Water (MW), Labrador Sea Water (LSW), lower North-East Atlantic Deep Water (NEADWI) and Eastern Reykjanes Ridge Current (ERRC). Four basins are delimited by grey dashed vertical lines. From Greenland to the coast of Portugal: Irminger basin (IrB), Iceland basin (IcB), East – North Atlantic basin (ENAB) and Iberian Basin (IbB).

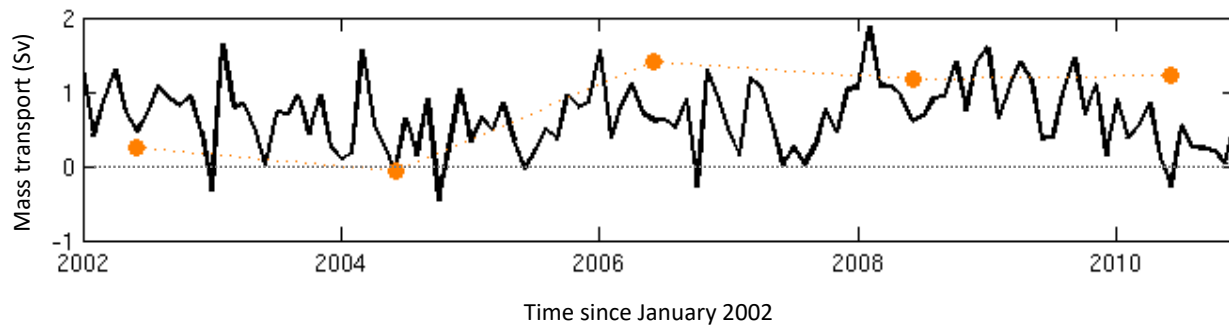


Fig. 4. Monthly evolution of the net volume transported across the Greenland-Portugal OVIDE section (Sv): model output (black continuous lines) and estimates derived from the OVIDE data set (orange dots) over the period 2002-2010

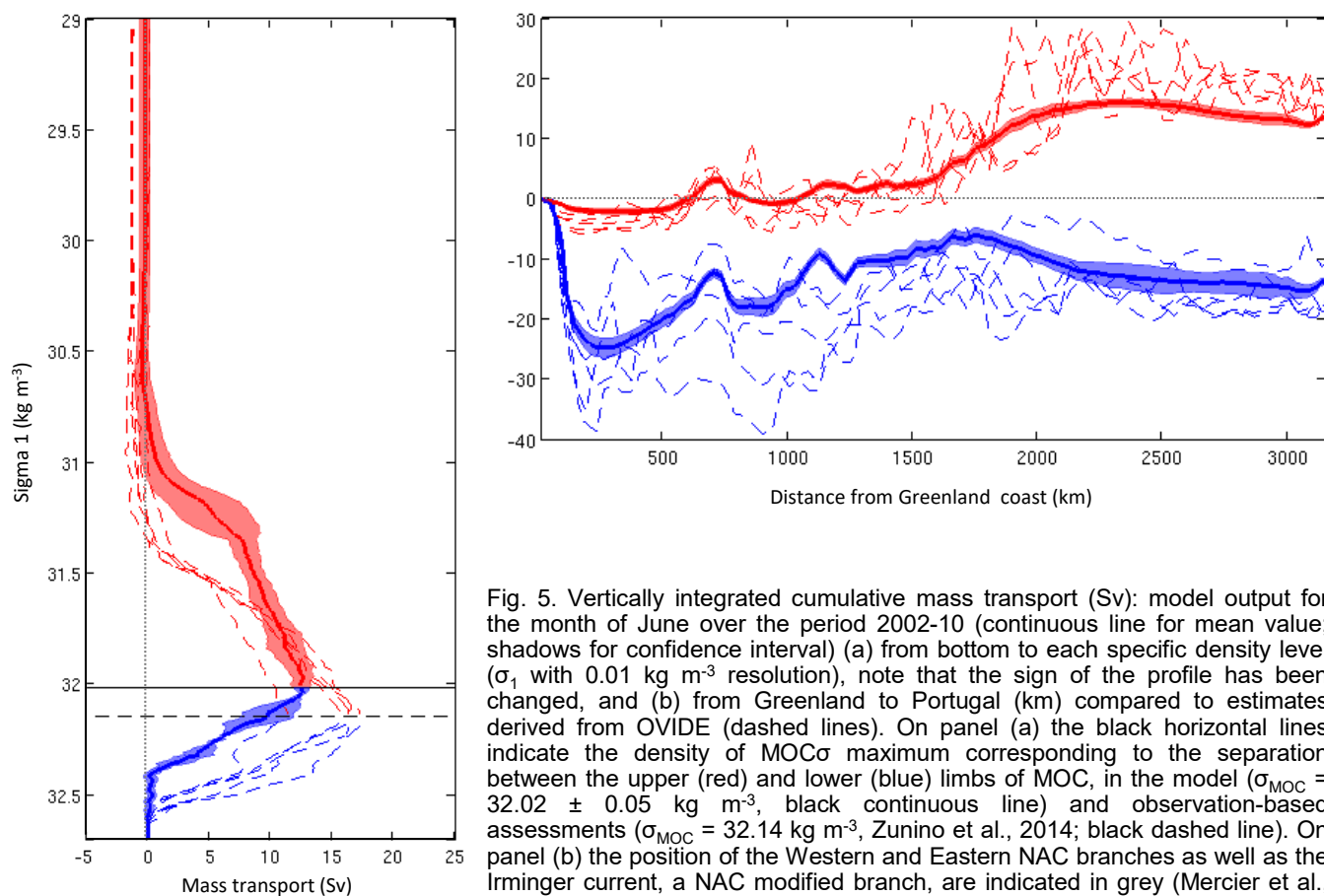


Fig. 5. Vertically integrated cumulative mass transport (Sv): model output for the month of June over the period 2002-10 (continuous line for mean value; shadows for confidence interval) (a) from bottom to each specific density level (σ_1 with 0.01 kg m^{-3} resolution), note that the sign of the profile has been changed, and (b) from Greenland to Portugal (km) compared to estimates derived from OVIDE (dashed lines). On panel (a) the black horizontal lines indicate the density of MOC σ maximum corresponding to the separation between the upper (red) and lower (blue) limbs of MOC, in the model ($\sigma_{\text{MOC}} = 32.02 \pm 0.05 \text{ kg m}^{-3}$, black continuous line) and observation-based assessments ($\sigma_{\text{MOC}} = 32.14 \text{ kg m}^{-3}$, Zunino et al., 2014; black dashed line). On panel (b) the position of the Western and Eastern NAC branches as well as the Irminger current, a NAC modified branch, are indicated in grey (Mercier et al., 2015).

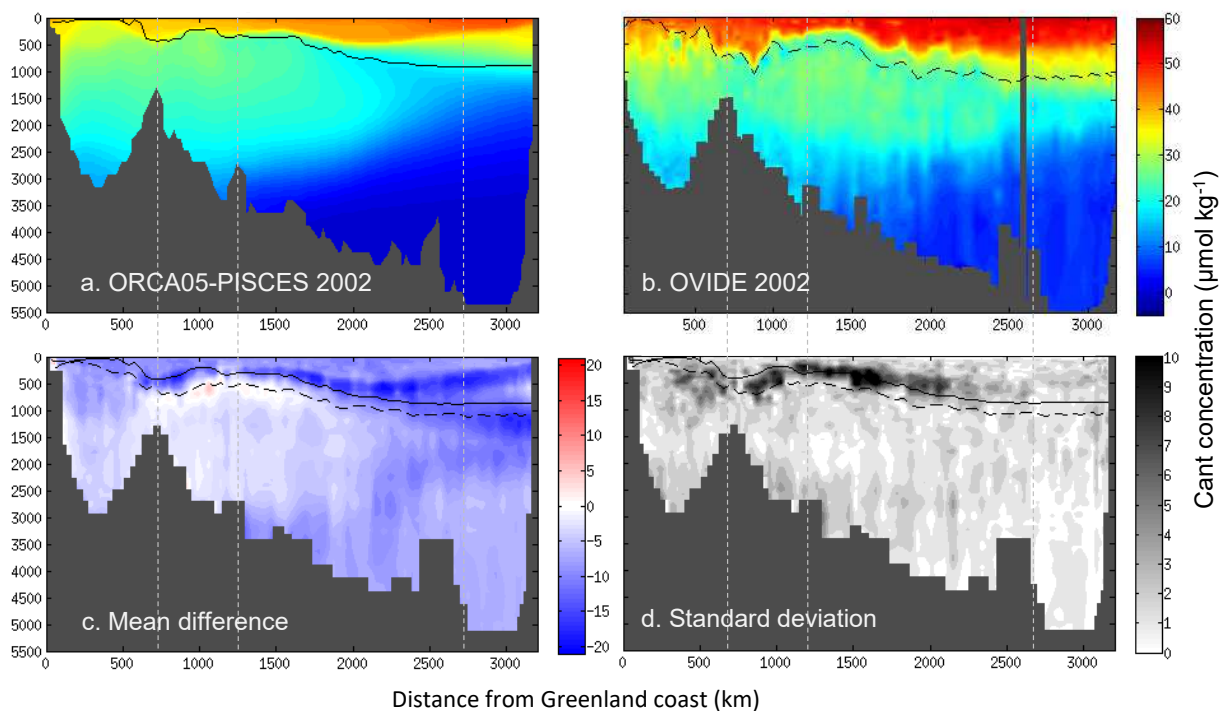


Fig. 6 : Water column distribution of anthropogenic C concentrations ($\mu\text{mol kg}^{-1}$) along the Greenland-Portugal OVIDE section in June 2002: (a) model output and (b) as estimated from the OVIDE data set. The difference between these both assessments (model – OVIDE) over the OVIDE period (June 2002-04-06-08-10) and its standard deviation are displayed on figures (c) and (d). Grey dashed lines delimit the four basins identified on figure 3. Black continuous and dashed lines indicate the limit between the upper and the lower limbs of the MOC in the model and the OVIDE data set.

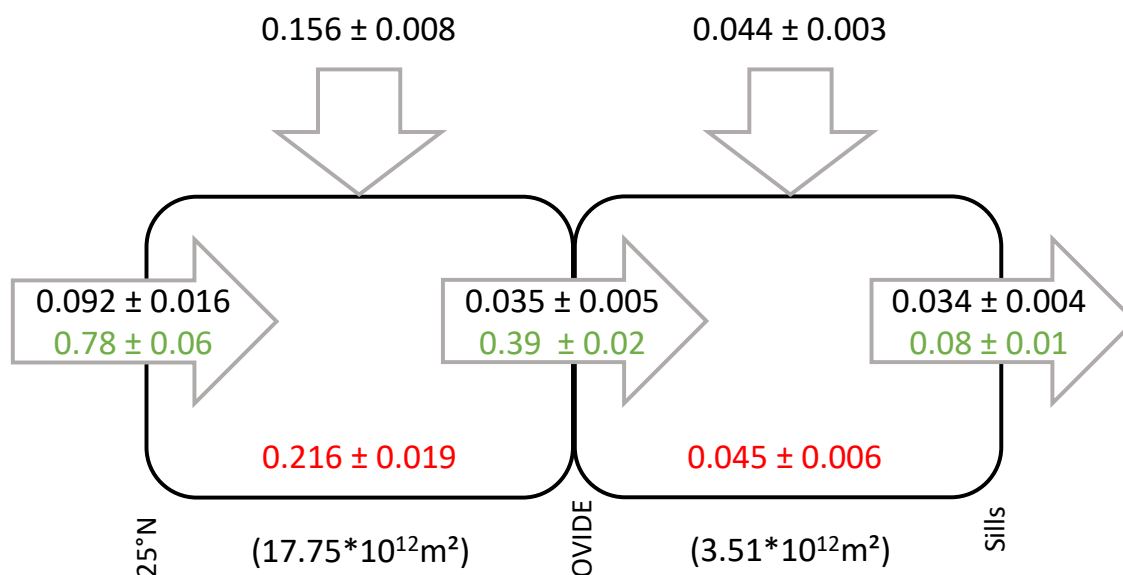


Fig. 7: Anthropogenic C budget of the Subtropical and Subpolar North Atlantic regions over the period 2003-2011. Average values and their standard deviation were estimated from smoothed time series. The horizontal arrows show the lateral Cant transport in PgC yr⁻¹ (black font). Red numbers in the panel indicate the Cant storage rate in PgC yr⁻¹. The vertical arrows show the anthropogenic air-sea CO₂ fluxes in PgC yr⁻¹. Green numbers represent the heat transport across sections in PW. Boundaries and surface area (m²) of each box are indicated below the panels.

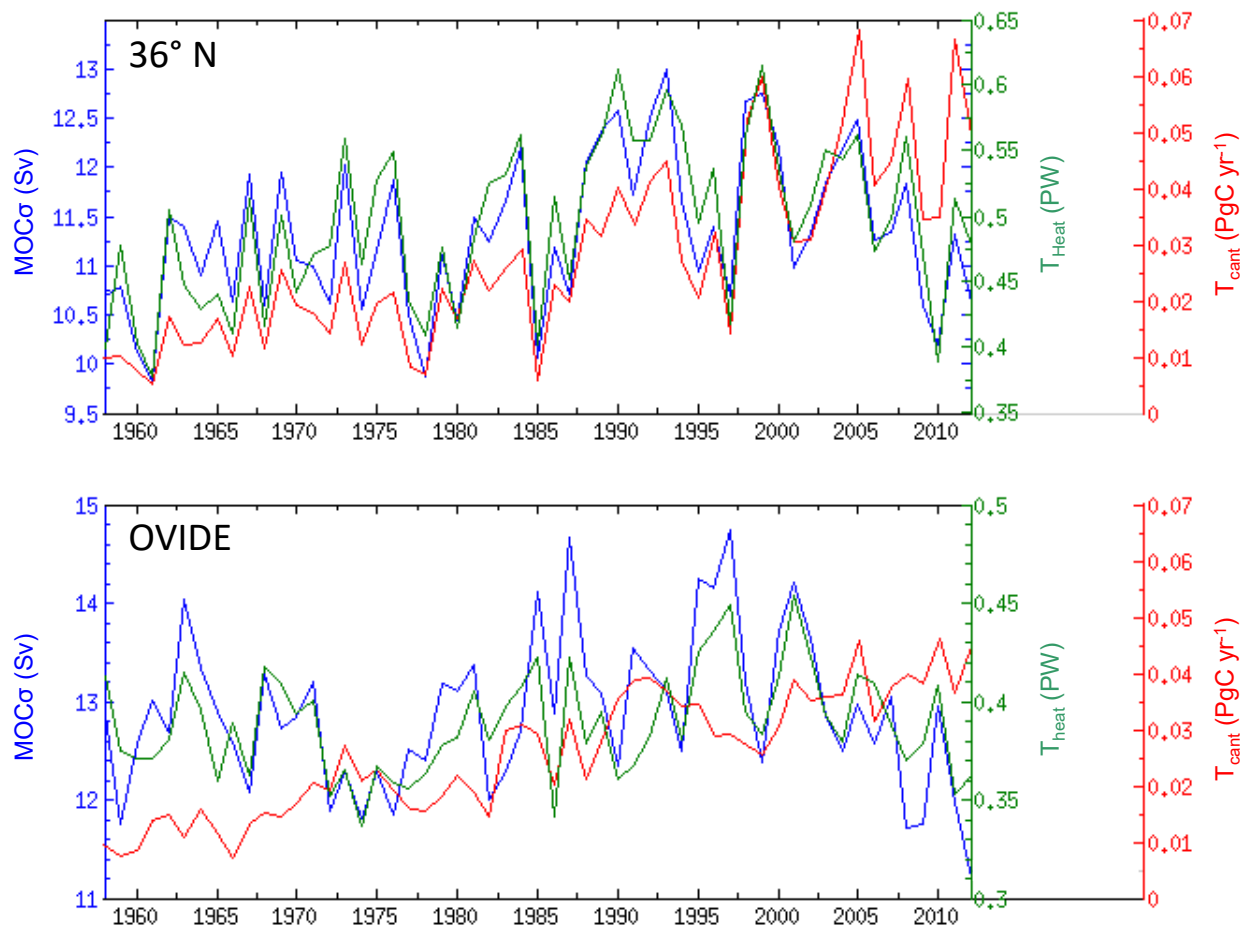


Fig. 8: Simulated annual time series of MOC magnitude ($MOC\sigma$, Sv) and transport of heat (PW) and anthropogenic C ($PgC\ yr^{-1}$) at $36^\circ\ N$ and at the OVIDE section estimated over the period 1958-2012.

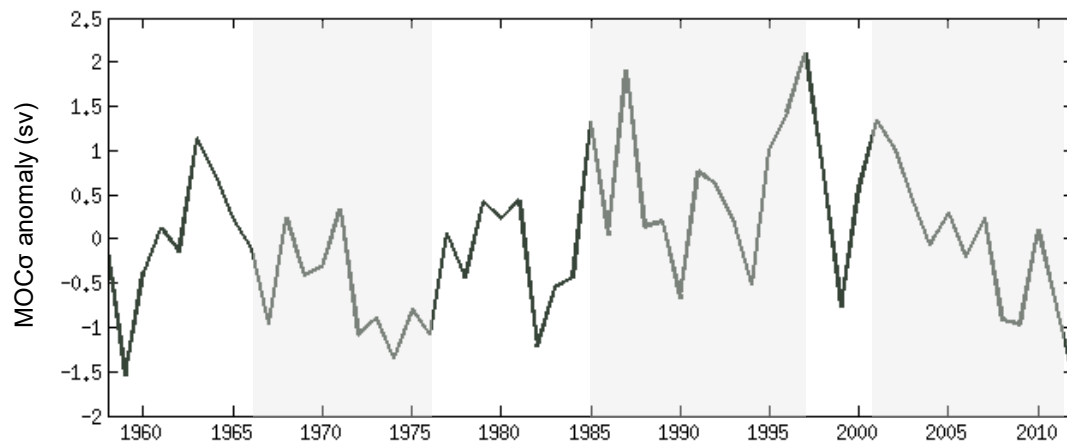
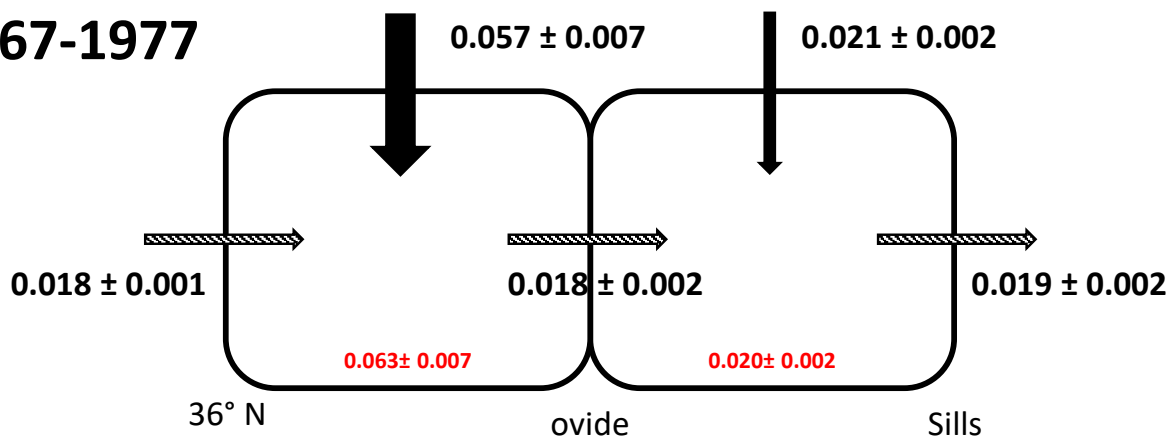


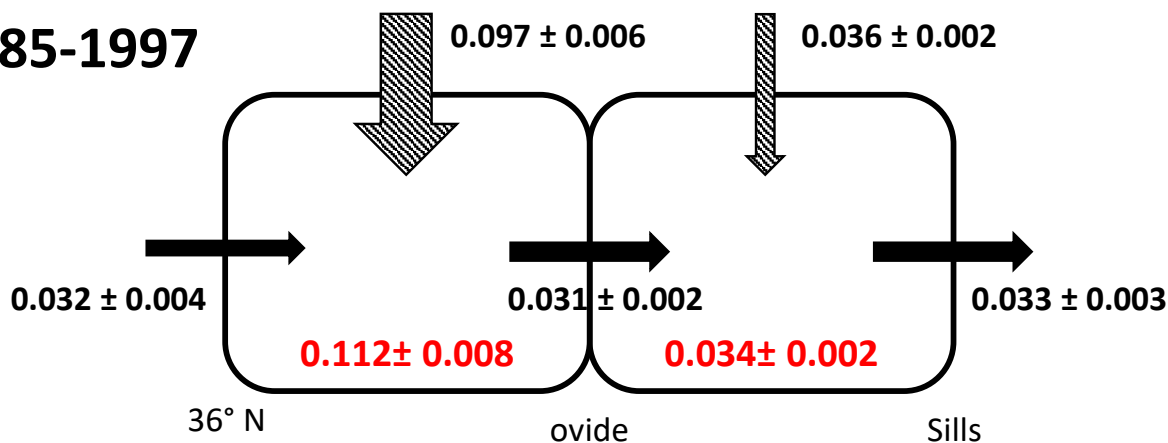
Fig. 9: Simulated annual time series of MOCσ anomaly over the period 1958-2012 along the Greenland-Portugal OVIDE section. Three particular periods are highlighted by grey areas: 1967-77 characterized by a weak MOCσ (negative MOCσ anomaly), 1985-97 with a strong MOCσ (positive MOCσ anomaly) and since 2002 (negative trend in MOCσ).



1967-1977



1985-1997



2002-2006

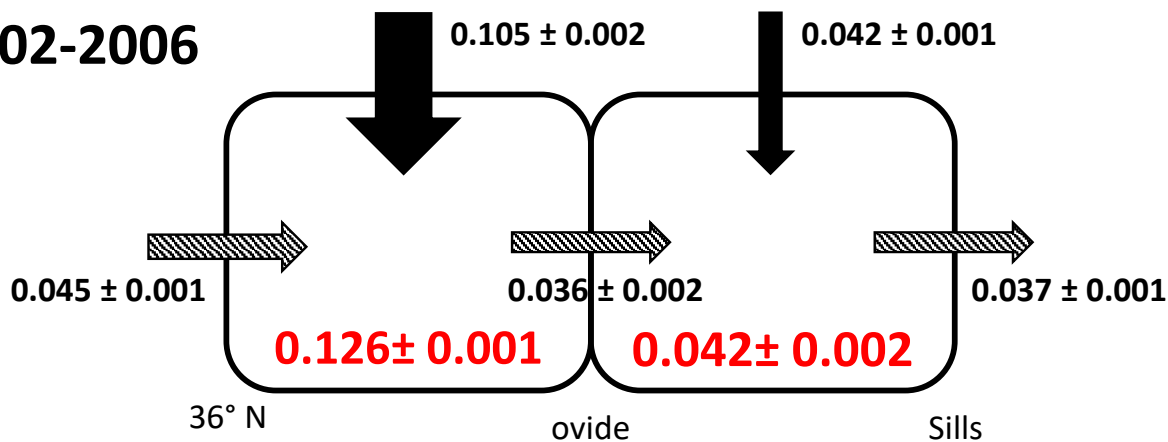




Fig. 10: Anthropogenic C budget for the period 1967-1977 (weak $MOC\sigma$), 1985-1997 (strong $MOC\sigma$) and 2002-2006 ($MOC\sigma$ negative trend) in the Subpolar North Atlantic region defined from 36° N to Nordic sill and divided in two boxes by the OVIDE section. Average values and their standard deviation were estimated from smoothed times series (Fig. S3). Vertical arrows show the air to sea anthropogenic CO_2 fluxes in $PgC\ yr^{-1}$, black horizontal arrows correspond to the advective transport of Cant across section in $PgC\ yr^{-1}$. Red numbers indicate the Cant storage rate in each box. The size of arrows and fonts used for the storage rate are proportional to the 2002-2006 budget. Hatched arrows indicate a strong correlation between the term and the regional Cant storage rate over the period of interest.